ATOMISTIC SIMULATIONS OF HYDROGEN EMBRITTLEMENT IN PALLADIUM

A Dissertation

by

HAN LENG

Submitted to the Office of Graduate and Professional Studies of
Texas A&M University
in partial fulfillment of the requirements for the degree of

DOCTOR OF PHILOSOPHY

Chair of Committee,	Tahir Cagin
Committee Members,	Xiaofeng Qian
	Miladin Radovic
	Benjamin Wilhite
Head of Department,	Ibrahim Karaman

December 2017

Major Subject: Materials Science and Engineering

ABSTRACT

Palladium hydrogen system has unique catalytic activities and up to 1:1 hydrogen adsorption capability. It is studied in the context of hydrogen embrittlement, which is a subset of stress corrosion cracking, with classical molecular dynamics techniques. Hydrogen embrittlement is a long lasting metallurgical challenge due to its intractability and unpredictability.

First, the thermomechanical properties are studied parametrically in a wide range of hydrogen concentration and temperature, serving a database for hierarchical multiscale simulations and constitutive models in mechanics. To quantitatively describe the kinetics of hydrogen segregation at crack tips, anisotropic diffusion properties are investigated under tensile/compressive loads in both elastic and plastic regions at different temperature and hydrogen concentration. Meanwhile, vacancy concentration as a function of strain is also studied in the same circumstances to quantitatively study the super abundant vacancy phenomenon and how it could initiate hydrogen embrittlement. Further, hydrogen interactions with coherent twin boundary is simulated at finite temperature. The local strength of twin boundary with hydrogen is estimated by molecular dynamics nanoindentation. At last, the heterogeneous nucleation mechanisms of defects under the influence of hydrogen content in single crystal pillars with different growth orientations are investigated to reveal the slip versus twin competition in plastic deformation. In short, a wide range of interesting topics are rigorously explored in the realm of atomistic hydrogen embrittlement.

ACKNOWLEDGEMENTS

I would like to thank Dr. Tahir Cagin for his guidance over the last four years at Texas A&M University. He not only inspired me to study physics, but also assisted me to develop a more matured personality. He is my dad in TAMU. I would like to thank my committee members, Dr. Xiaofeng Qian, Dr. Miladin Radovic, and Dr. Benjamin Wilhite. I appreciate Dr. Wilhite who showed tremendous patience and dedication to our collaboration. Thanks also go to my friends Dr. Jin Li, Dr. Jie Jian, Dr. Zhe Fan, Dr. Gang Yang, Yi Wang and Bo Wang. Same for my colleagues Dr. Sevil Sarikurt, Richard Gustafson and Lan Huang. Also, the department faculty and staff Dr. Li Liu, Dr. Lisa Perez, Jules Henry, Haley Nigg and Amy Caldwell. Special thanks for Dr. Qian, Dr Radovic, Dr. Liu, and Dr. Perez for the academic guidance and patience.

Finally, thanks to my mother and father for their encouragement and patience.

CONTRIBUTORS AND FUNDING SOURCES

Contributors

This work was supervised by a dissertation committee consisting of Professor Tahir Cagin and Professor Miladin Radovic and Professor Xiaofeng Qian of the Department of Materials Science and Engineering and Professor Benjamin Wilhite of the Department of Chemical Engineering.

All work conducted for the dissertation was completed by the student independently.

Funding Sources

There are no outside funding contributions to acknowledge related to the research and compilation of this document.

TABLE OF CONTENTS

Page

LIST OF FIGURES

Page

LIST OF TABLES

Page

1. INTRODUCTION

1.1 Origins

The perspective of this thesis can be set from the Environmental Assisted Cracking (EAC), a specific category of corrosion which will lead to the drastic decaying of mechanical properties. EAC typically includes Stress Corrosion Cracking (SCC)[1], Hydrogen-Induced Cracking (HIC), and liquid Metal Cracking (LME). Hydrogen-induced damages can be further categorized into hydrogen embrittlement (HE)[2-9], hydrogen induced blistering, crack from precipitation of internal hydrogen, hydrogen attack, and hydride formation. Most of the hydrogen related mechanisms do involve with phase transformation and can be prevented properly with standard treatments, except for HE, which is elusive and hard to be stopped. So far, HE is vastly studied in steel industry[10, 11] in engineering composition-processing-structural-properties relationship, same for Ni[12], Co, Fe-based superalloys, Ti alloys, and Al-based alloys. In terms of applications, steels in petrochemical refinery, hydrogen tanks in automotive, nuclear waste disposal, nuclear power plant, pressure vessels and pipes for storage and transport are the major victims. Further, aero-engineering and marine-engineering are also suffered from HE.

From another perspective, palladium[13-21] (Pd) has been heavily studied due to its critical roles in the future hydrogen economy. Its unique catalytic[22-25] and hydrogen absorbing properties[6, 7, 26, 27] have made it a strong candidate in hydrogen purification, hydrogen storage as a capping layer, hydrogen detection as sensors, and fuel cell catalysis by alloying with platinum (Pt). Here, both HE and Hydride formation should be carefully analyzed for Pd. Meanwhile, it is one of the members in the platinum group, which includes the most expensive also the rarest elements in the earth crust. They are excellent catalysts because of the characteristic forms of d orbitals. Pt, for instance, can help transfer ammonium into nitric-acids. It is also the key component in fuel cells, which power the hydrogen vehicles.

1.2 Processes

The schematic of the hydrogen embrittlement processes[28-38] is shown in Fig 1.1[39]. The overall sequence is absorption, diffusion, interaction and failure.

Hydrogen can be absorbed from hydrogen dipoles as gas, from solutions as protons, or through the chemical reactions from hydro-compounds. In the processes of thermal forming, i.e. forging, casting, and welding, extra-care must be drawn with the preclusion of hydrogen. Elimination of the source of hydrogen is an effective way of stopping hydrogen embrittlement. Thus, understanding the inclusion processes of hydrogen are critical. DFT method[2, 4, 40-43] is suitable for the study of these processes. However, they are not the focus in this thesis. One of potential study direction would be the hydrogen shielding by ceramic coating combined with high throughput calculations.

After the hydrogen atoms are absorbed, protons diffuse into the materials and settle at the positions with local energy minimum. The protons will preferentially stay in the area with defects where open volumes are available. These include lattice interstitial sites, grain boundaries, dislocations, vacancies, voids, and interface between matrix and precipitates. Depending on where the protons locate and the interactions with defects, the accumulative influences from these micro events toward the macroscopic materials response will be different.

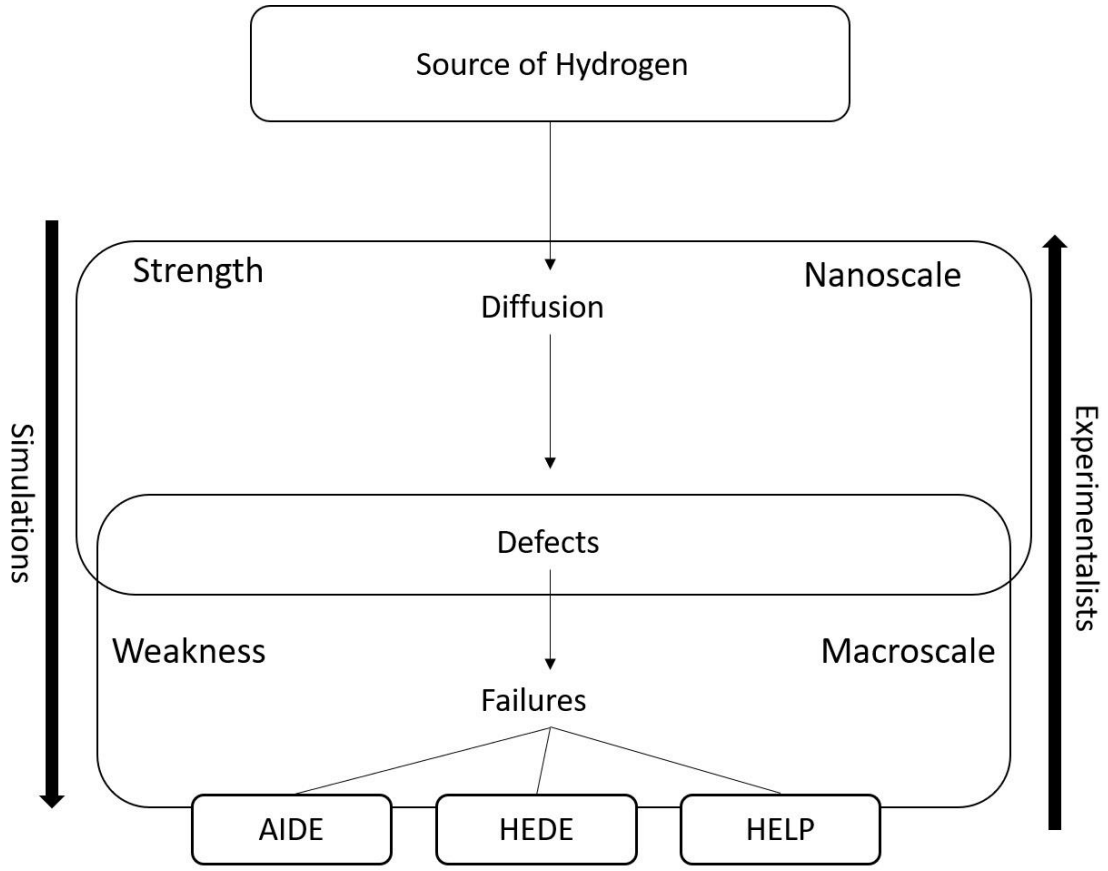

Figure 1.1 Schematics of Hydrogen Embrittlement processes.[39]

1.3 Deformation Mechanisms

Despite the challenges, there are a couple hypothetical failure mechanisms are proposed for engineering materials, as shown in Fig. 1.2. Engineering materials are defined as bulk parts which are vastly produced through hot forming techniques including casting, rolling, forging, welding etc. A detailed overview of these failure mechanics due to hydrogen embrittlement can be found in the reference[44]. Here, Hydrogen Enhanced Local Plasticity (HELP) [31, 35], Adsorption Induced Dislocation Emission (AIDE) [45], and Hydrogen Enhanced Decohesion (HEDE) [46] will be briefly introduced. A schematic with engineering mechanisms and cooperation between them are shown in Fig. 1.2. For thinfilms and nanostructured materials, dislocation theory based nanomechanics[47, 48] are

used to characterize the effect of hydrogen embrittlement[49]. Recently, hydrogen induced super abundant vacancy (SAV) [50, 51] effects is proposed to be a new hydrogen embrittlement mechanism. Also, a newly innovated hypothetical phase change induced cracking mechanism will be discussed.

In HELP, due to hydrogen localization near crack tip and hydrostatic stresses, plastic deformation will be focused at the crack front due to the hydrogen facilitated dislocation activities. Crack path could be either transgranular or intergranular depending on the microstructure at crack front is either the grain interiors or grain boundaries. Specifically, both dislocation nucleation and dislocation migration are enhanced by the localized hydrogen concentration combined with the hydrostatic stress.

According to AIDE, the absorbed hydrogen might facilitate the nucleation and migration of dislocations at surfaces away from the crack tips. It also involves the nucleation and growth of nano-voids in front of the crack. Voids formation facilitates crack growth, also resharpen the crack-tip.

The HEDE theory, with charge transfer from 1s orbital of H to the d orbital of the metals, weakens the bond between lattice atoms. It is a sequential tensile separation of atoms at crack tips when critical crack-tip-opening displacement (CTOD) is reached. Incipient shear movement of atoms are involved to enable the CTOD. Dislocation activities may be limited so that the crack tip is continually sharp. HEDE tend to happen at 1) Atomically sharp crack tips due to adsorpted hydrogen. 2) Several tens of nanometers ahead of the crack where dislocation shielding effects results in a local tensile stress maximum. 3) Positions of maximum hydrostatic stress (several um for high strength steel) 4) Particle-matrix interfaces at the crack-front.

The SAV based theory indicates that hydrogen vacancy complexes are very stable can block dislocation gliding. The amount of vacancy in the system is linearly proportional to the product of flow stress and strain[51]. As the amount of vacancy grows, they tend to combine with each other to form nanovoids. These nanovoids might later become cracks or become energetically favorable so that crack will preferably approach towards.

Here, I propose a hypothetical theory, which is stress induced phase transition in the metal-hydrogen phase diagram. This is highly possible, especially in spin related elements, e.g. Fe and Ni. Since their phase diagram tend to be very complicated. It is possible, that stress induced phase change might convert the previously ductile phase into a much softer or brittle phase. To prove this hypothesis, one should extend phase diagram calculations into another dimension, i.e. pressure. This could be done by density functional theory combined with Monte Carlo simulations[52]. This is by itself a Ph.D. thesis, if the details of vibrational entropy etc. are considered. By no means to underestimate the difficulty in this topic, here, there is no attempts to prove this hypothesis.

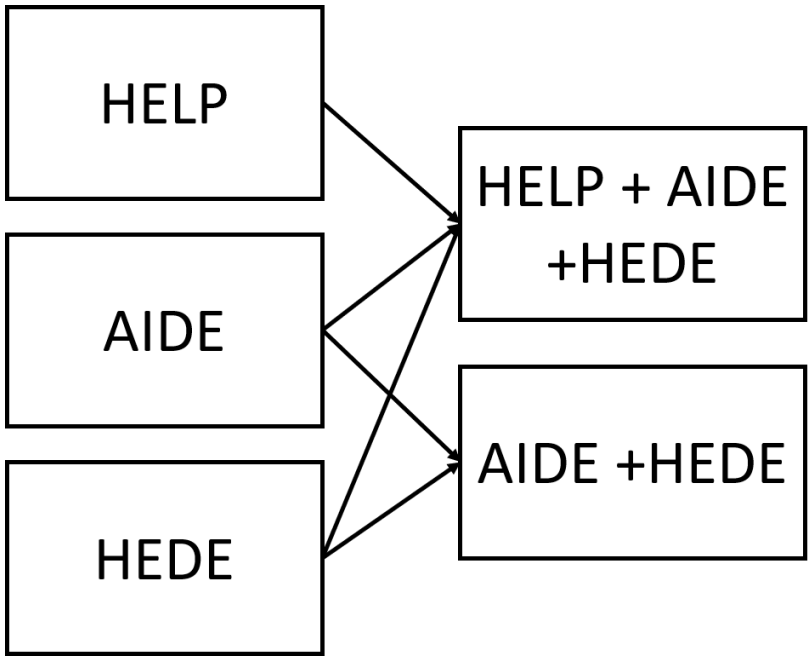

Figure 1.2 Schematics of HE failure mechanisms.

1.4 Approaches

The approach we propose is: merging materials science with solid mechanics via atomistic simulations. To link the nanoscale with mesoscale, understanding and

cooperation of the following fields are necessary. Hydrogen embrittlement has been a long lasting metallurgic challenge in engineering, experimental, and simulations. Engineering wise, part failure caused by HE are highly unpredictable during the manufacture, storage, and service processes. It is also hard to trace the history of stress load and environmental influence on parts. When HE is studied by material science experimental approaches, either failed parts or lab-fabricated samples can be prepared for various characterization techniques. The microstructural images of at different stages of deformation processes combined with the stress-strain curves are quite informative. However, special and time resolutions are still remaining challenges. The in-situ deformation techniques are still at their early stage. Meanwhile, atomistic simulation can also offer some insight about the individual microscopic events which constitute the HE phenomenon. However, with the limited time duration and special dimensions, the cumulative effects of micro-events in a realistic strain rate and sample size are not available. Also, systems involve with magnetism and more than two elements cannot be described by classical pair-wise or pair-functional potentials so far. Continuum simulation methods have difficulties describing diffusion and stress induced phase and defect behaviors at the crack front. These are a summary of the challenges to solve HE issue.

Never the less, as a compromise, the energetics and kinetics studies of the diffusion processes and hydrogen interactions with lattices and defects in the background of crystal plasticity are suitable topics for atomistic simulations[53, 54]. This will be the main approach applied in this thesis.

1.4.1 Experimental Techniques

Although experimental studies[55] of HE are costly and the hydrogen defect interactions in atomistic level are hard to be characterized, most of the contributions towards the understanding of hydrogen embrittlement are coming from experiments. Newly evolved techniques such as SEM/TEM fractography and in situ deformation tests are very powerful that qualitative, even quantitative results are becoming possible in nanoscales. The main concern from the industry has always been in steels, which are very

complicated systems with multiple phases combined with complex forming processes. Besides, the requirement for the experimental set-up is rigorous. For example, 5 ppm level of O_2 in the environment can greatly slow down the crack propagation processes in steel, varying the observations.

On the other hand, the way metallurgists study the mechanical failures by implementation of fractography can be regard as “reverse engineering”, i.e. deduction of the failure processes during the service lives based on the fractographic structure. Due to the lack of process information, it might be omitted that unpredictable events in the service lives may cause severe consequences.

1.4.2 Atomistic Nanomechanics (Simulations)

As atomistic simulations gradually become a mature field in late 1990s, study of binary solid systems with classical molecular dynamics (MD) has started, assuming the systems to be solid-solutions with limited solubility. The development of atomistic simulations potentially facilitates the investigation of the microscopic-origins of macroscale events. The strength of atomistic simulations is that the crystallography and dislocation theory can be applied to quantitatively analyze the well visualized results, enabling us to the understanding of the failure origins in atomic level, which is difficult to achieve through experiments[53, 54, 56, 57]. Both energetic and kinetic simulations will offer valuable data which determine the mechanical behaviors of materials. However, as mentioned before, there is a well-defined range for the capabilities of atomistic simulations. The solutions for extending our capabilities to the macroscale are available in two categories, i.e. (1) apply the multiscale simulation approaches to reproduce the crack propagation and interactions with materials, also the morphology of fracture surfaces and the mechanical strength of the material. (2) Utilize the atomistic simulations combined with constitutive laws/models in solid mechanics as levers to magnify the impact of the input results. Here, the second approach is preferred because modeling is a tool that can help us better understand the theories, but it is not the substitution of theories. Over-relying on simulations to reproduce every scheme or phenomenon is inappropriate.

1.4.3 Solid Mechanics (Theory)

Since solid mechanics are gradually developed from elasticity to plasticity and still basically stayed in continuous media. The discontinuities near the crack tip area raised tremendous difficulties until fracture mechanics becomes the trend. The constitutive laws and models developed for the analysis of mechanical failures should be regard as weapons in our arsenal. For example, calculating surface formation energy and applying the Rice-Wang theory is better strategy for understanding the influence of solute to the strength of the interface than directly running a fracture simulation[58]. Calculating generalized stacking fault energy can offer deeper understanding in deformation twinning and crystal plasticity than simply implement deformation simulations in molecular dynamics.

1.4.4 Critical Factors

There are many critical factors that need to be addressed.

1.4.4.1 Orientation

Orientation plays critical role in nano-structures' deformation processes. Mark Tschopp[59-74] et al. has performed a solid study on the orientation effect on bulk tension/compression properties with analysis of normal stresses and critical resolved shear stress (CRSS) on the principal slip planes.

1.4.4.2 Fracture Modes

Complex stress field and fracture modes[75-77] will be experienced during the deformation processes in nano-structures. The material behaviors under different fracture modes, especially mixed modes in atomistic level are interesting topics. Compare to the uniaxial tensile test, where stress strain curves are represented, crack velocity with respect to stress intensity factor would be a more precise description. Unfortunately, so far it is not appropriate in atomistic simulations.

1.4.4.3 Temperature

Density of point defects and dislocations are determined by temperature for materials in equilibrium state. Temperature also governs the rate of several kinetic processes, e.g. dislocation multiplication, cross slip, climb, mobility, intersection etc.

1.4.4.4 Strain Rate

Density and nucleation of defects, crack propagations and other kinetics processes are influenced by the strain rate. These will eventually lead to different mechanics behaviors of materials. Study of defect activation volumes[78-80] can indirectly elucidate the strain rate sensitivities of materials.

1.4.4.5 Defects

The study of the interactions between point, planar, and volumetric defects[81-89] are critical but challenging. The related studies have enhanced our understandings of materials mechanics. In nanoscale, unique properties are emerging, e.g. defect behaviors are different from the bulk materials. My favourite authors in this section includes but not limited to: Ju Li[47, 90-96], Ting Zhu, and Van Swygenhoven [97, 98].

1.5 Challenges

The current debates are focused on whether the dissolved hydrogen or adsorbed hydrogen are the major cause of the failures, whether the failures are caused by decohesion or localized slip mechanisms, and the role of vacancy in the fracture processes.

So far, there is no experimental techniques for resolving atomistic crack-tip processes in bulk materials. Studies are over-ambitious, focusing on commercial materials in complex environments. Atomistic/multi-scale modelling of crack growth is not yet sufficiently realistic. The fundamental mechanisms are buried and blurred by all the other influences. Different mechanisms are predominating for different fracture modes, so that consistent conclusions are hardly reached.

At last, a special appreciation is given to projects including Materials Genome Initiatives (MGI), Integrated Computational Material Engineering (ICME), and Predictive Integrated Structural Materials Science (PRISMS), for the enlightenment and benefits.

2. ATOMISTIC SIMULATION

2.1 Overview

Atomistic simulations include static calculations and dynamic calculations. The level of theory could be based on quantum mechanics and classical mechanics. For quantum mechanical methods, applications for quantum chemistry normally use spherical coordinates. For inorganic materials, plane wave approximation is widely accepted. Static calculations are useful for predicting the energetics of events in nanoscales. With harmonic approximation, the free energies can be calculated for low temperature region. Dynamic calculations can study thermomechanical properties of varies systems at different temperatures. By applying Green-Kubo relationship, transport properties can also be obtained. Furthermore, some scenarios where non-equilibrium dynamics simulations are needed. For quantum mechanics, density functional theory is currently most widely used. For classical mechanics in inorganic materials, embedded atom method potentials are the main stream, especially for metals.

2.2 Molecular Dynamics (MD) Simulation

Molecular dynamics is a calculation scheme which follows Newton's second law. For each particle in the system, the energy can be calculated by an expression of potential energy, which is a function of particle positions. The force on each particle can be calculated by the derivative of potential energy with respect to the position related parameters. When random velocities is assigned and the periodic boundary condition is applied, the internal energy, number of particle, and volume of the system are fixed. To control the pressure and temperature, different ensembles can be applied to change the constant thermodynamic conjugate parameters. Equilibrium molecular dynamics is preferred against non-equilibrium molecular dynamics in this thesis, considering that the fundamental Liouville 's theorem is based on the assumption of system equilibration.

2.3 Embedded Atom Model (EAM) Force Field

Embedded atom model is a pair-wise functional potential developed by Daw and Baskes[99], It is good for simulations with vacancies and open surfaces and its design theory is very similar to density functional theory. The potential energy expression for EAM potential is composed by a density functional term and a pair-wise term. The density functional term takes the hypothetical electronic density as input and outputs an embed energy. The merit of EAM potential is its low computational cost and the decent accuracy for many defects simulations and calculations of mechanical properties. For most of the potentials available, there is a specific range (could be very narrow) of applications that they are good for. And it is predetermined during the developments. It is essential to have a good understanding of the potential before using them. Besides Daw and Baskes, Yuri Mishin should be also mentioned as his copper potential[100] has offered excellent performance in most of the plasticity applications, setting a standard for the future EAM potential developers.

3. THERMAL MECHANICAL PROPERTIES

3.1 Overview

For atomistic simulations, hydrogen interactions with local defects such as dislocations[3, 49], vacancies[5, 51], grain boundaries[8] and etc. are well suited problems and can offer information about the atomic origin of HE. But the focus of the community is on Fe[10, 11] and Ni[12], in which the solubility of hydrogen is limited. On the other hand, atomistic simulations also excel in calculating thermomechanical properties, from which implications can be obtained with well proved constitutive laws and models, leading to a better understand of HE. For instance, M. Gillan[57] studied the diffusion properties of a system with 108 palladium atoms and 20 hydrogen atoms from 500K to 1000K by molecular dynamics (MD). Y. Li and G. Wahnstrom[53] did similar work with 256 Pd atoms and 8 H atoms at 623K. Zhong et al.[54] calculated the young's modulus and tensile properties of hydrogen-palladium system. Due to the difficulty of correctly describe the high solubility and consequent hydride formation process by classical potentials in MD, neither the variation of hydrogen concentration nor the hydrogen diffusivities under critical temperature were included in these pioneer works. The mechanical behaviors can only be regard as valid in elastic regions since the dislocation activities were confined. Also, Ab initio method have also been utilized to study the quantum mechanical effects underlying the HE mechanisms[40], e.g. the energetic studies of transition states of H in various lattice positions[41, 42], including vacancies and crystal defect sites[2, 4, 43].

Recently, the development of Embedded Atom Method (EAM) potentials[99] has enabled the correct description of phase behaviors of PdH systems for up to 100% H/Pd atomic ratio[101]. The purpose of this work is to study the thermomechanical properties with temperature ranges from 100K to 1900K and with up to 40% H/Pd atomic ratio under the correct influences of phase behaviors. The atomic trajectories are used to analyze the hydrogen diffusion activities, its hopping events and the strains in the surrounding Pd atoms. We found that Young's modulus drops monotonically as hydrogen concentration increases at temperatures above 300K. Mechanical destabilization is predicted at 40%

atomic ratio and 700K. The diffusion activation energy drops by 18% when the atomic ratio changes from 1% to 40%. The hydrogen inclusion has the peak enhancement to the hydrogen hopping ratio at 500K. By applying the thermal ellipsoid analysis, pre-melting of Pd lattice has been observed at H concentration above 30% atomic ratio at 900K. We suggest that our data and conclusions have enhanced the foundation for the quick evolving multiscale simulations and have implications to the understanding of the hydrogen embrittlement in general. In this work, the material behaviors and properties under the influence of hydrogen aggregation, which normally occurs in front of crack tips, have been demonstrated. The change of properties might have a profound impact on the hydrogen induced crack propagations.

3.2 Simulation Method

Classical molecular dynamics method is implemented by Large-scale Atomic/Molecular Massively Parallel Simulator (LAMMPS)[102] with Embedded Atom Model (EAM) potential[101] to simulate PdH system. The total energy in EAM potential consists of an embedded energy functional and the pair wise function as shown in equation 3.1.

$$E = F(\rho_i) + \frac{1}{2}\sum_{ij}^{i \neq j} \varphi(r_{ij}) \tag{3.1}$$

It has been proven that the right phase stabilities and mechanical properties of the PdH system can be represented. We constructed a 20x20x20 FCC supercell with 32000 Pd atoms and periodic boundary conditions in x, y and z directions. Hydrogen atoms were randomly inserted into octahedral sites.[103] The time step was chosen to be 0.5 fs to match the hydrogen vibrational frequencies. The Nose Hoover thermostat and barostat were implemented with the temperature damping parameter as 50 fs and the pressure damping parameter as 500 fs. For result analysis, thermodynamic data and trajectories data were recorded each 1 fs and 100 fs, respectively. It was verified that there is minor difference between the diffusion coefficients of hydrogen calculated from trajectories exported with 10 fs and 100 fs intervals.

The initial temperature of 1K was given to the system by Gaussian distribution. Subsequently, we increased the temperature from 1K to 1900K with 100K temperature increment each cycle (the experimental melting point of Pd is 1828.15 K[104]). For each cycle, temperature was first increased by 100K with NVT ensemble in 10 ps followed by a 20 ps relaxation run, with NPH ensemble, to equilibrate the systems. Then, the thermodynamic and trajectory data was sampled for 100 ps with NPH ensemble. The approach of 10 ps changing, 20 ps relaxing, and 100 ps sampling scheme were used exclusively in this work.

For calculating mechanical properties, hydrostatic stress from 0.0, to 0.5, 1.0, 2.0, 3.0, 4.0, 5.0, 7.5, 10.0, 12.5, 15.0, 17.5, and 20.0 GPa was applied under NPT ensemble to obtain the bulk modulus. 5% and 3% strains were applied with NVT ensemble and 1% increment each time to obtain the tetragonal shear moduli and the pure shear moduli, correspondingly. The elastic moduli were then obtained through stress strain relationships. At last, uniaxial tensile deformations were simulated by applying the stress from 0.0 to -10.0 GPa, with 1 GPa as increment. The tensile stress was applied in Z direction, while X and Y planes were kept free under NPT ensemble.

3.3 Thermodynamic Properties

With regard to the thermodynamics properties under influences, previous study claimed that the inclusion of hydrogen had a similar effect as the increment of temperature to the properties of Pd[54]. It has practical standing points since most of the applications of PdH system are above the critical temperatures. The change of melting point can reflect the varied hydrogen palladium interactions. Thermal expansion coefficient is critical to materials degradation because of the large lattice expansions. Heat capacities data is corresponding to the temperature differential spectroscopy (TDS) results, which is effective for the study of hydrogen trapping[9]. Thus, the joint effect of temperature and H/Pd atomic ratio from 0-40% to the thermodynamics properties are studied.

The melting points for the PdH systems is obtained by conducting a second cycle of heating with 25K increment (Fig. 3.1a). Lattice constants as a function of temperature

and hydrogen concentration are shown in Fig. 3.1b. Our MD results show that the melting temperature of pure palladium is around 1400K whereas the experimental value is 1828.15K[104]. The data was fitted to the polynomial $f(x)=A_0*x^2+B_0*x+C_0$ where x is the H/Pd atomic ratio. Results show that A_0 is 0.151467, B_0 is -18.6283, and C_0 is 1387.88 K. The melting temperature dropped 12.5K as the H concentration increased by 1%. The positive pre-factor A_0 indicates that the melting temperature will drop slower as the H content increases.

The volumetric thermal expansion coefficients α_p and isobaric heat capacities C_p are defined in equation 3.2 and equation 3.3. Their values at different hydrogen concentrations and temperatures are shown in Fig. 3.2a and Fig. 3.2b, respectively.

$$\alpha_P = \frac{1}{V_0}\left(\frac{\partial V}{\partial T}\right)_P \tag{3.2}$$

$$C_P = \left(\frac{\partial H}{\partial T}\right)_P \tag{3.3}$$

The non-linear behaviors of α_p and C_p, as shown in Fig. 3.2, can be explained by the difference of hydrogen interactions mechanisms in alpha phase and beta phase at different temperature and H content in the context of the phase diagram of PdH[24]. In both phases, hydrogen atoms stay in octahedral sites, with a H/Pd atomic ratio of 0.03 and 0.60 at room temperature. As the critical point for PdH system is at 566 K, and 26% atomic ratio, the proportion of alpha and beta phases can be calculated by the lever rule when temperature and composition are within the coexistence boundary. And the miscibility gap is disappeared when temperature and composition are beyond the coexistence boundary. The inclusion of hydrogen is decreasing the curvature of both thermal expansion coefficient and heat capacities as a function of temperature, indicating that PdH bonds are eliminating the increment of the thermal expansions and lattice vibrations as temperature increases, especially when both temperature and H content are high.

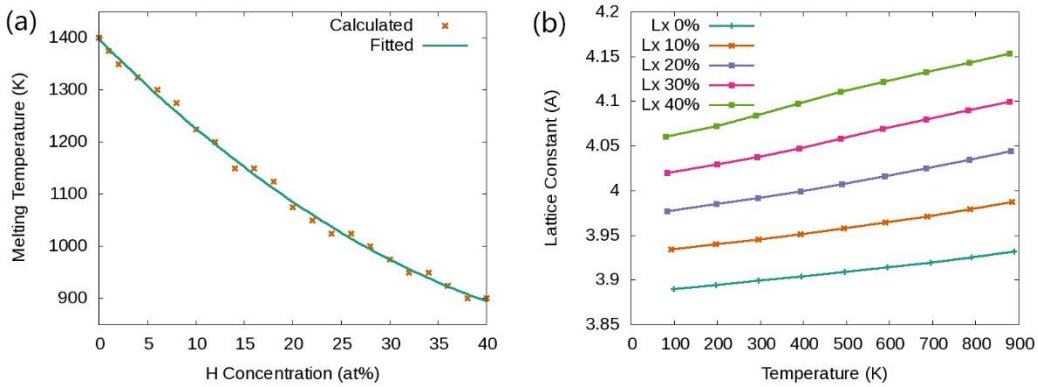

Figure 3.1 (a) Melting temperature of the PdH system as a function of hydrogen concentration at ambient pressure. (b) The lattice constant as a function of hydrogen concentration and temperature. The solid lines correspond to the fitting functions while the molecular dynamics results are shown as points.

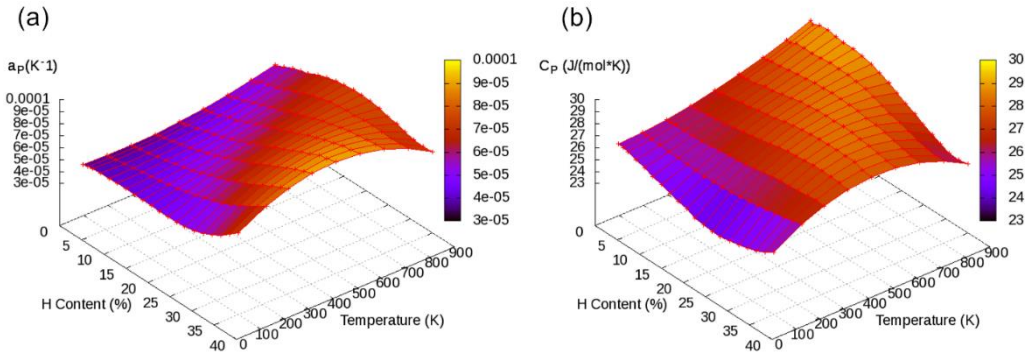

Figure 3.2 (a) Volumetric thermal expansion coefficient and (b) isobaric heat capacity of the PdH system as a function of hydrogen concentration and temperature at ambient pressure.

3.4 Mechanical Properties

Parametric studies of mechanical properties were carried out from 100K to 900K and with 0-10% H/Pd atom ratio. The results provide direct input dataset for simulation method in large scales, e.g. dislocation dynamics. Also, they can be used as input for

constitutive models to obtain other properties of the material. In this work, the independent elastic constants for FCC metals, i.e. C_{11}, C_{12}, and C_{44}, are obtained from the stress strain relationship. The bulk modulus is deduced from Rose-Vinet equation of states[105].

The results of C_{11}, C_{12}, C_{44} and Bulk Modulus as a function of temperature and H content are shown in Fig. 3.3(a), Fig. 3.3(b), Fig. 3.3(c) and Fig. 3.3(d), respectively. The results are then fitted to a polynomial in the form of $F(H, T) = A_0H+B_0T+C_0HT+D_0$ with fitted parameters shown in Table 3.1. The elastic constants and bulk modulus show a monotonic degradation as the temperature and H concentration increase. At 0K for pure Pd system, C_{11}=257.4 GPa, C_{12}=209.95 GPa, C_{44}=55.1 GPa and B=225.76 GPa. As temperature increased by 100K, the C_{11} drops 6.814 GPa (2.64%), C_{12} drops 6 GPa(2.86%), C_{44} drops 2.9 GPa (5.26%) and B drops 6.277 GPa (2.78%). As H concentration increased by 1%, the C_{11} drops 1.918 GPa (0.745%), C_{12} drops 1.47 GPa (0.7%), and C_{44} drops 0.87 GPa (1.58%). However, the correlated effect of temperature and H content, which is represented by C_0, is small for all four moduli. Mechanical destabilization is predicted to occur when we extrapolate the system state to 700K and 40% H/Pd ratio, and the value of C_{44} is approaching 0 GPa. The low resistance to shear deformation will lead to the early failure of the material.

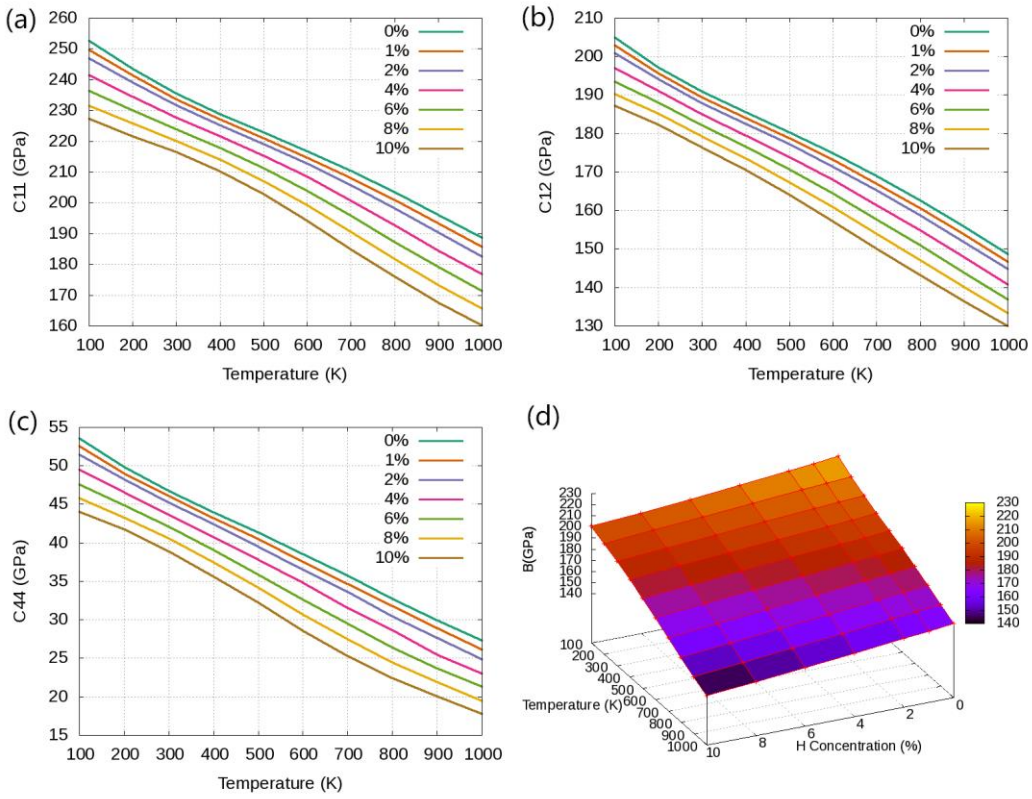

Figure 3.3 Elastic constants (a) C11, (b) C12, (c) C44, (d) bulk modulus of the PdH system as a function of hydrogen concentration and temperature.

Table 3.1 The fitting parameters of a third order polynomial of elastic constants Cij (GPa).

Elastic Constant	A_0	B_0	C_0	D_0
C_{11}	-1.9181	-0.06814	-0.00083	257.379
C_{12}	-1.46972	-0.06	-0.00046	209.945
C_{44}	-0.87	-0.029	-0.000152	55.1064
Bulk Modulus	-1.61922	-0.06277	-0.00058	225.756

Besides, uni-axial tensile simulations were implemented to the systems with 0-10% H/Pd ratio and at temperatures of 300K, 500K, 700K and 900K, as shown in Fig. 3.4(a), 3.4(b), 3.4(c) and 3.4(d), respectively. The Young's moduli were obtained through the slop of the stress strain curves. At 300K, our results matched with the work done by W. Zhong[14], i.e. the hydrogen inclusion doesn't affect Young's modulus. However, as the temperature of the system raised to 700K and 900K, the effect of hydrogen inclusion on Young's modulus become more pronounced and Zhong's conclusion failed beyond the near room temperature region.

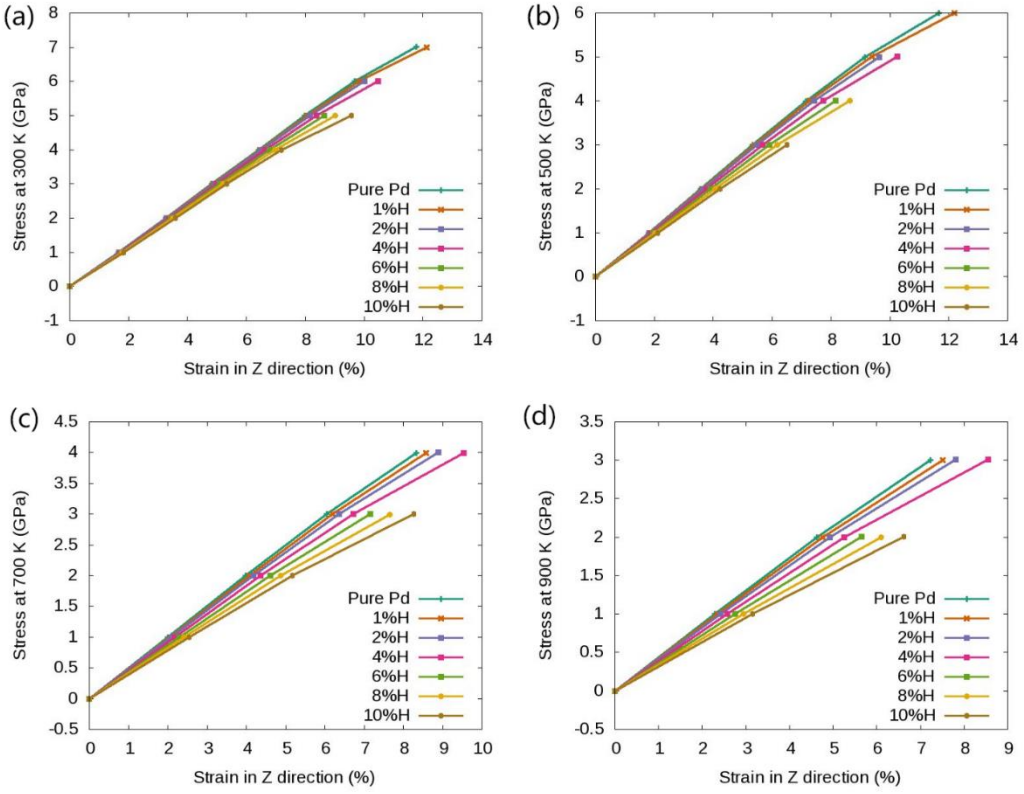

Figure 3.4 Stress strain relationship at (a) 300K, (b) 500K, (c) 700K, (d) 900K for tensile simulations in z direction for the PdH system as a function of hydrogen concentration from 0 to 10%.

3.5 Hydrogen Diffusion

Traditionally, the influence of solute concentration on diffusivity is considered to be negligible. We measured the averaged diffusivity of the H atoms from 100K to 900K, with H/Pd ratio from 1% to 40%, by using the mean squared displacement (MSD) method, shown as following.

$$D = \lim_{t\to\infty} \frac{1}{6tN} \sum_{i=1,N} \left\langle \left| r_i(t) - r_i(0) \right|^2 \right\rangle \tag{2.1}$$

where t is the time step, N is the number of hydrogen atoms.

The Arrhenius plots of diffusion coefficient show that the hydrogen concentration enhances the hydrogen diffusion at low temperature regions (Fig. 3.5(a)). It changes from $2*10^{-7}$ cm^2/s to 10^{-6} cm^2/s when the H/Pd ratio goes from 1% to 40% at 200K. The influence of concentration to the diffusivity becomes smaller when the temperature gets beyond 300K. For instance, at 1000K, the hydrogen diffusivity obly varies from $5.601*10^{-4}$ cm^2/s to $5.86*10^{-4}$ cm^2/s as the H/Pd ratio changes from 1% to 40%.

Further, we calculated diffusion activation energy, Q_d. The fitting results of diffusion activation energies are shown in Fig. 3.5(b), in which the value of D_0 is fixed to the experimental value of 29 cm^2/s[56]. Q_d drops from 0.16 eV in dilute solution to 0.14 eV at higher concentration because of the lattice expansion, which opens up the diffusion path for hydrogen atoms.

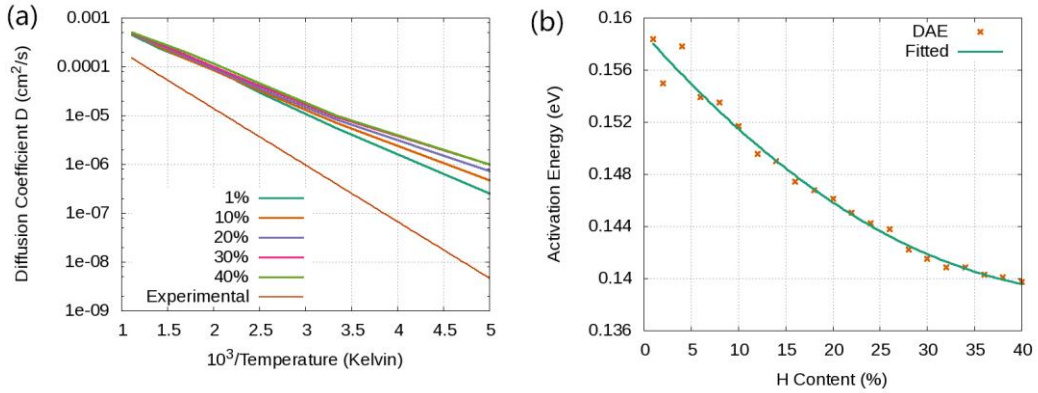

Figure 3.5 (a) Diffusion coefficient and (b) diffusion activation energy of hydrogen in palladium as a function of hydrogen concentration and Temperature.

The diffusion path of hydrogen is from octahedral (OC) site to tetrahedral (TC) site, then to octahedral site in Pd. The ratio of hopping events with respect to vibrational events for the hydrogen atoms determines their diffusion rate. A hydrogen atom is determined as hopped atom if it travelled more than $\sqrt{3}a/4$ in 100 fs. The time averaged results are summarized in Table 3.2 and it shows the ratio between hopped hydrogen atoms and total hydrogen atoms at different concentrations and temperatures. Below 300K hopping events happen less than 1% regardless the hydrogen concentration. From 500K to 1300K, the values of hopping ratio changed with different H/Pd ratios. And the lower the temperature, the more obvious the changes, as shown in the column with percentage difference of the hopping ratio, i.e. $(H_{38\%}-H_{2\%})/H_{38\%}$. The maximum difference shown at 500K, which also proved that what we observed for heat capacity and thermal expansion coefficients are consistent, i.e. the hydrogen palladium interactions are most active from 400K to 500K.

Table 3.2 Selected hopping ratio at hydrogen concentration of 2%, 20% and 38% at 500K, 700K, 1000K, and 1300K.

Temperature	$H_{2\%}$	$H_{20\%}$	$H_{38\%}$	$(H_{38\%}-H_{2\%})/H_{38\%}$
500K	7.5%	9%	11%	31.82%
700K	18%	21%	25%	28%
1000K	36%	40%	42%	14.3%
1300K	50%	56%	57%	12.3%

The vibrational magnitude of the Pd atoms, which accompanied with surrounding H atoms, are calculated through thermal ellipsoids as a function of temperature and H content. The thermal ellipsoid values of Pd atoms which are not accompanied by H atoms are excluded with a cutoff radius of 2.45 Å. Thermal ellipsoid is the standard deviation of the coordinates of atoms in a 3x3 matrix. They reflect the enhancement of vibrational magnitude of each Pd atom caused by the surrounding H atoms, which is directly related to the mechanical stability.

$$\begin{bmatrix} \sigma_{xx} & \sigma_{xy} & \sigma_{xz} \\ \sigma_{yx} & \sigma_{yy} & \sigma_{yz} \\ \sigma_{zx} & \sigma_{zy} & \sigma_{zz} \end{bmatrix} \tag{2.2}$$

in which $\sigma_{xx} = \langle x^2 \rangle - \langle x \rangle^2$; $\sigma_{xy} = \langle x \cdot y \rangle - \langle x \rangle \cdot \langle y \rangle$ etc. We calculated the square root of them and plotted in Fig. 3.6.

The result shows that the influence of H atoms to Pd atoms is enhanced linearly as the temperature gets higher in both xx and xy directions (Fig. 3.6). The magnitude of σ_{xx}, σ_{yy}, and σ_{zz} are identical, and so as the σ_{xy}, σ_{yz}, σ_{zx}, showing isotropic character. The

magnitudes of orthogonal terms are around 50% larger than those of the off-diagonal terms. When H/Pd ratio is 30% and temperature is above 900K, discontinuity occurs in both σ_{xx} and σ_{xy} as an indication of local melting. The rate of atom switching position is directly related to diffusion related mechanical relaxation. It is the key to the creep related properties.

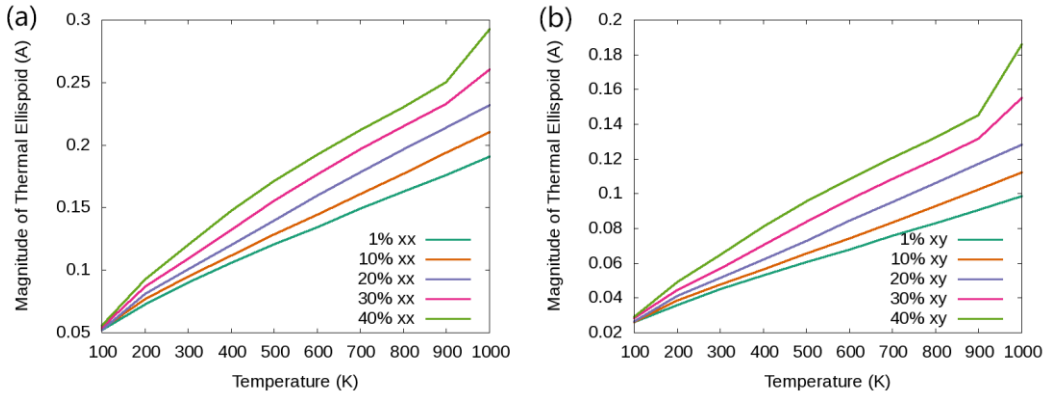

Figure 3.6 Thermal ellipsoid elements (a) diagonal element xx and (b) off-diagonal element xy for the Pd atoms adjacent to H atoms at different temperature and H concentrations.

3.6 Conclusion

Classical molecular dynamics calculations implemented by Large-scale Atomic/Molecular Massively Parallel Simulator (LAMMPS)[102] are carried out with a PdH EAM potential[101] to study the fundamental thermomechanical properties of Pd single crystal as a joint effect of temperature and hydrogen inclusion. A 32000 atoms Pd single crystal with periodic boundary condition is used. The thermodynamic properties such as melting point, heat capacity and thermal expansion coefficient are studied, as well as the mechanical properties which include elastic constants and Young's modulus. Also, diffusion related properties including the diffusivity, diffusion activation energy, hopping ratio of hydrogen atoms are investigated. At last, hydrogen induced premelting is observed by the technique of thermal ellipsoids, which is also an indication of creep behaviors.

Results show that hydrogen concentration has strong effects on Young's modulus, diffusivity, diffusion activation energies and other properties. We suggest that our conclusions have enhanced the understanding of the detrimental effects induced by the concentrated hydrogen, which is normally observed in front of the crack-tips where hydrogen embrittlement takes off. Our data can also serve as input dataset for the quick evolving multiscale simulations of hydrogen influenced crack propagations.

4. ANISOTROPIC DIFFUSION UNDER UNI-AXIAL DEFORMATION

4.1 Overview

PdH system sustains high stresses and strains during the hydrogen absorption and desorption processes.[25] To remedy the problems, researches have been conducted on the mechanical properties and hydrogen diffusion processes of the system.[53, 54, 56, 57] But the complexity is considerable because while the mechanical deformation and stress concentrations are affecting diffusion process, the biased diffusion activities of hydrogen are also influencing the mechanical properties and the deformation processes through its interactions with Pd.[106] Dederich et al. proposed analytical models of hydrogen diffusion under elastic strain in perfect lattices.[107] However, the analytical solutions are not capable of depicting the complex phase behaviors embedded in PdH system. The effect of mechanical deformation on the hydrogen diffusion process in Pd has been rarely studied. Besides, defects will generate unique strain/stress field around them. In these unperfected local areas, the diffusion process and energetic landscape will be different from those of perfect crystals.[108] While the interactions between different defects and hydrogen atoms have been studied[22], the details of how the hydrogen diffusivity will be influenced by the existence of dislocations in the PdH system under plastic strain is remained unexplored. In this work, we studied the influence of uni-axial tension and compression on the diffusion process in a bulk single crystal PdH system.

While the in-situ experimental study of the correlation between mechanical load and hydrogen diffusion is challenging, the subject is well suited for classical equilibrium molecular dynamics, which is implemented by Large-scale Atomic/Molecular Massively Parallel Simulator (LAMMPS)[102] for this study. The EAM potential in use is developed by XW Zhou et al[109], which has successfully predicted the phase order, hydrogen diffusion process, and mechanical properties of the PdH system.

4.2 Simulation Method

The basic Pd Face Centered Cubic (FCC) single crystal matrix was constructed as 20x20x20 supercell with 32000 Pd atoms. The initial crystals were created based on the lattice constant a=3.8849 Å associated with the potential.[109] Periodic boundary conditions were applied in all x, y and z directions which were pointing at the <100> directions. All the samples were adequately deformed from 0% to 16% strain uni-axially to cover both the elastic and plastic regions. Constant strain was applied in z direction while the x and y planes were kept at stress free. The hydrogen atoms were randomly put into octahedral sites. The time step was 0.5 fs to catch the hydrogen vibrational motions. The Nose Hoover thermostat and barostat were used to control the temperature and pressure[110], in which the temperature damping parameter is chosen to be 50 fs, and the pressure damping parameter is 500 fs. The temperature was brought up to 1000K in 10 cycles. For each cycle, temperature was first increased by 100K within 10 ps followed by a 20 ps relaxation run to equilibrate the systems. Then the system was sampled by extracting the thermal and trajectory data for 100 ps with NPT ensemble. The same approach was applied in mechanical deformation processes, where the strain is increased with 1% increment each cycle. Diffusion coefficients in x, y, and z directions, i.e. D_{xx}, D_{yy}, and D_{zz} were calculated by mean square displacement (MSD) method, as shown in equation 4.1. As strain is applied in z direction, D_{zz} is defined as $D_{//}$ as it was parallel to the z direction. D_{xx} and D_{yy} are denoted as $D_{\perp}$, perpendicular to the z direction.

$$D = \lim_{t\to\infty} \frac{1}{2tN} \sum_{i=1,N} \left| x_i(t) - x_i(0) \right|^2 \tag{4.1}$$

The deformation simulations are carried out at 100K, 300K, 500K, 700K, and 900K to study the influence of temperature as well. In general, the diffusivity increases as temperature gets higher according to:

$$D = D_0 \exp\left(-\frac{Q_d}{k_B T} \right) \tag{4.2}$$

The elasto-diffusivity have been well studied by Dederichs et al.[107] And the diffusion tensor of a cubic crystal under homogeneous deformation can be expressed by:

$$D_{ij} = D_0\delta_{ij} + \sum_{kl} d_{ijkl}\varepsilon_{kl} \tag{4.3}$$

in which ε_{kl} is the strain field, d_{ijkl} is the elastodiffusion tensor, δ_{ij} is the delta function, and D_{ij} is the diffusion tensor, which is diagonal in cubic crystals.

4.3 Diffusion

The diffusivity as a function of temperature and strain are shown in Fig. 4.2 for both tension and compression cases. The snap shots of plastically deformed microstructures for both tension and compression cases are shown in Fig. 4.1.

In the elastic region, most of the systems we studied have shown a parabolic relationship between the diffusivities and applied strains. Meanwhile, their behaviors also vary as a function of temperature. At 100K, hydrogen atoms in all the samples are vibrating at their interstitial sites, stay at their local positions, while $D_{\perp}$ and $D_{//}$ are almost unchanged before yielding for both tension and compression cases. In between 300K and 900K, both $D_{//}$ and $D_{\perp}$ for tension samples are increasing as deformation proceeds. But $D_{//}$ is increasing faster than $D_{\perp}$. The discrepancy between $D_{\perp}$ and $D_{//}$ is proportional to the temperature when it is below 500K. Above 500K, the discrepancy is fixed, becomes irrelevant to temperature. On the other hand, when the compression is applied, $D_{\perp}$ is increasing slightly when the temperature is below 500K. At 700K and 900K, $D_{\perp}$becomes decreasing. $D_{//}$is always increased parabolically under compression. The discrepancy between $D_{\perp}$ and $D_{//}$ is proportional to the temperature from 100K to 700K.

The hydrogen concentration has less impacts than the applied strain to the diffusivities. Higher concentrations would smooth the diffusivity curves as more hydrogen atoms are sampled for the average values. And its influence to the mechanical properties, e.g. the yield strength, affects the diffusivity indirectly. In the elastic regions, the

maximum discrepancy between $D_{\perp}$ and $D_{//}$ is normally reached when yielding takes place, at which the highest elastic stresses are loaded. The following plastic deformations will lead to the decrease of three properties, i.e. the system stresses, the scalar values of diffusivities, and the difference between $D_{\perp}$and $D_{//}$.

Depending on the material responses in plastic deformations, for instance, the nucleation of dislocations and the subsequent stress relaxation, three schemes were summarized. First, if the defect density is large enough, then the elastic stress will stay in low values. Consequently, the values of $D_{\perp}$and $D_{//}$ will be almost identical and close to the original value (of system with no strain) as the system is further deformed. One of the examples is Fig. 4.2 (b), i.e. the tensile process for 2% PdH system at 300K. Second, if the defect density is not dense enough or the dislocations are piled up in more complicated cases, the deviation of diffusivity in different directions can still be observed after yielding since a certain level of the stresses are remained in the system. For instance, the tensile process for 6% PdH system at 500K. Third, if the stresses keep increasing as the material is further deformed after yielding, the deviation of diffusivities will again be enlarged, until the next defect (dislocation) is triggered to release the stresses and elastic strains. It was illustrated as in the tensile process of the 6% PdH sample at 300K.

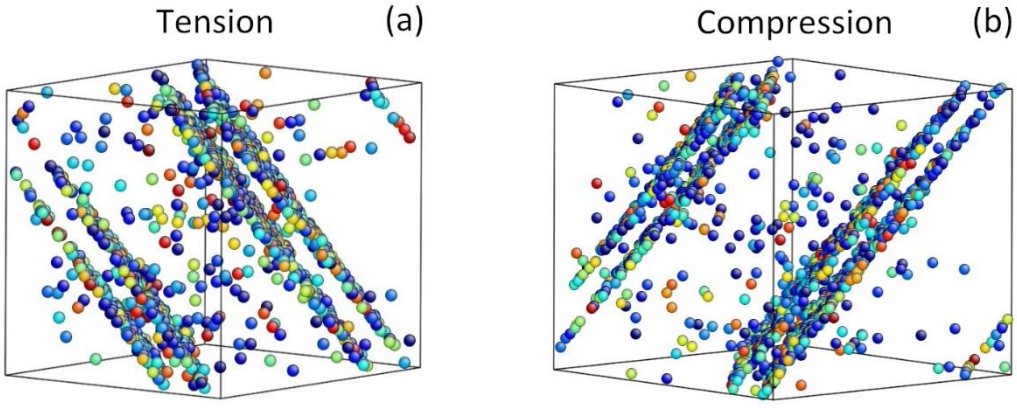

Figure 4.1 Formation of dislocations from yielding during (a) tension and (b) compression process, at 700K, 9% deformation strain and 10% hydrogen content. The dislocations are formed in (111) planes. Only palladium atoms which have high centro-symmetry are visible, the hydrogen atoms are hidden for clarity.

Overall, diffusivity tends to restore quickly to the original values at zero strain state, may be in the next 1% or 2% deformations when temperature is between 300K and 500K. However, at 700K and 900K, the diffusivities are more likely to restore to the original value in a slower motion, e.g. in around the next 5% deformations after the critical points. A hypothetical explanation to the temperature effect is that small strains (less than 4% strain) have minor effect at 300K on the directional diffusivity during the elastic deformation, so this also applies to the plastic deformation process, i.e. the diffusivity as a vector is not that sensitive to the stresses at 300K. However, at temperature higher than 500K, the diffusivity is more sensitive to small stresses. And therefore the remained stresses in the plastic deformation processes at higher temperatures can have a more profound effect on the diffusivities.

For FCC metals, diffusion path is from octahedral site, to tetrahedral site, then to octahedral site. Between octahedral sites and tetrahedral sites, the displacement of hydrogen atom is (±1/4a, ±1/4b, ±1/4c), where a, b, c are the length of the lattice constants. They are identical at zero stress. However, under uni-axial tension and compression, their values are changed and depending on the strain values and poison's ratios. So, the diffusivities are proportional to the strained lattice constants in elastic regions. However, exceptions are observed for both tension and compression processes. In tension, $D_{\perp}$ is still increasing when corresponding lattice parameters are shrinking. In compression, $D_{/\!/}$ is increasing at 300K, but gradually deceases at 700K and 900K.

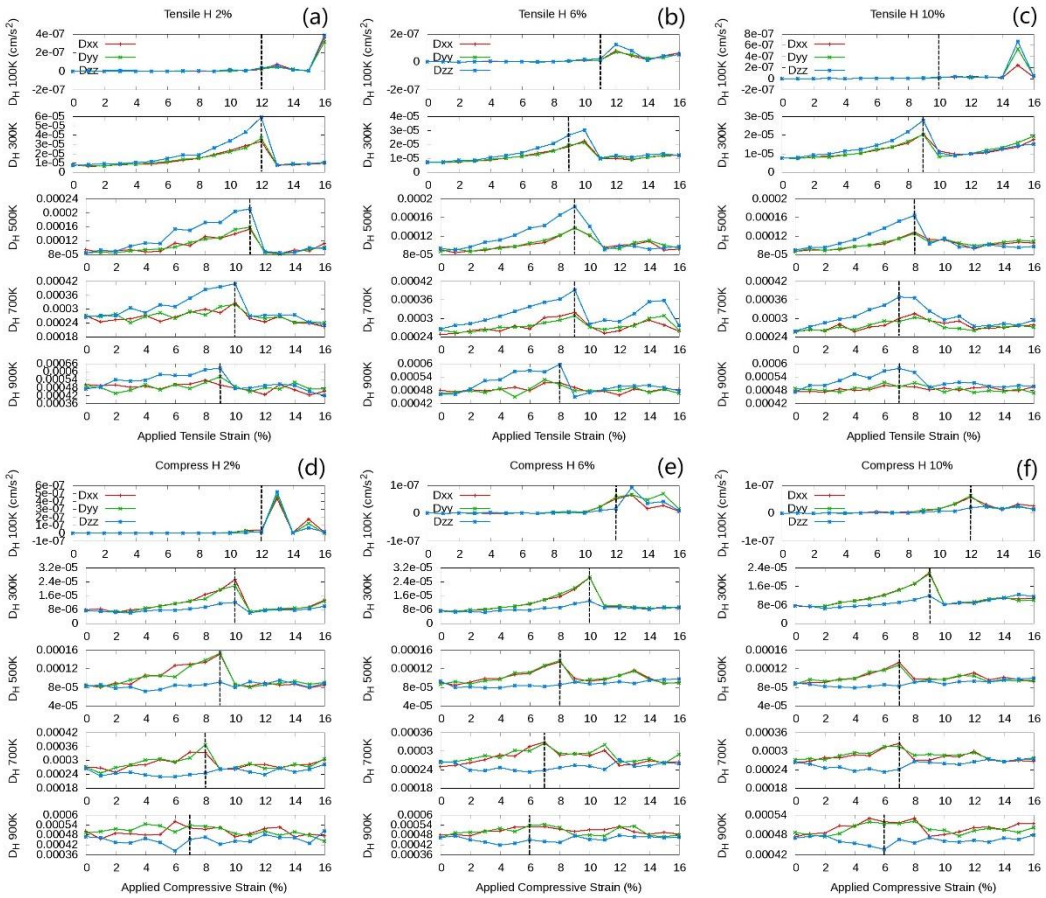

Figure 4.2 Diffusion coefficient in xx, yy, zz directions of PdH system under different tensile load, temperature, and hydrogen concentration. (a, b, c are for tension, d, e, f are for compression.) The vertical dash lines are indicating the critical tensile strain.

4.4 Conclusion

In summary, classical molecular dynamics method has been applied to study the anisotropic hydrogen diffusion behaviors under tension and compression strain in palladium. During the elastic region of the tension processes, diffusivity in all directions are increased, but the one along loading directions will get larger as the strain is applied, while the perpendicular vectors are increased slower. During the elastic compression processes, the diffusivity along the compressing direction will increase at 300K, remain unchanged at 500K, and decrease at 700K and 900K. The other two directions will have

major increments. The yield strain of both the tension cases and the compression cases will have decreased by increasing the temperature and hydrogen concentration. In the plastic region for both cases, the derivation of diffusivities are governed by the remained stresses in the system, which are depending on the dislocations nucleation and evolutions.

5. VACANCY CROWDING UNDER DEFORMATION

5.1 Overview

Fukai et al[111] found that the inclusion of hydrogen will also increase the vacancy concentration. And the hydrogen will enter the vacancy to form hydrogen vacancy complex (HVC), a thermodynamically stable and low diffusivity structure unit, causing vacancy crowding, or the super abundant vacancy (SAV) effect. Although the phenomenon of super abundant vacancy has been known from 1993 and intensive studies have been done in the next ten years[112-118], the correlation between the high concentrations of vacancies have not been seriously considered to be the source of nano-voids formation, which will be critical for crack nucleation and propagation at regions with high stress concentrations. The influence of HVC to the plasticity was remain unknown. Recently, Suzhi et al[51] have proved by multi scale simulations combined with experimental works that the large amount of vacancy clusters and accompanied vacancy hydrogen complexes could accelerate the growth of nano-voids and have a great impact on the plasticity behaviors in front of the crack tips. Degang et al[50], on the other hand, proved that HVC can lock dislocations in aluminum, changing the plastic behaviors at the nano-pillars by the strong correlation and interaction between the dislocations and hydrogen-vacancies complexes. In present work, molecular dynamics method is implemented by Large-scale Atomic/Molecular Massively Parallel Simulator (LAMMPS)[102] to systematically study the influence of hydrogen concentration, temperature, and uniaxial tension/compression strains on the vacancy concentrations.

Vacancy concentrations[111-118] of PdH system as a function of uni-axial deformation, temperature, hydrogen concentrations are studied by molecular dynamics calculations. A 32000 atoms Pd single crystal with periodic boundary condition is used. With application of a novel vacancy detection algorithm[51], we found that hydrogen can facilitate the formation of vacancies at different temperatures. During elastic deformations, the vacancy concentration is a parabolic function of elastic strain. The hydrogen effect during mechanical deformation is not obvious when the hydrogen concentration is 1% but

becomes stronger at 10%. The mechanical, thermal, and hydrogen effects are well explained by the numerical models. Results implies that hydrogen vacancy complex might potentially change the material's mechanical behaviors from ductile to brittle.[50]

5.2 Simulation Method

The basic Pd Face Centered Cubic (FCC) single crystal matrix was constructed with 32000 Pd atoms as 20x20x20 supercell. The initial crystals are created based on the lattice constant a=3.8849 Å. An embedded atom model (EAM) potential[101], which can accurately represent the mechanical response of the PdH system, is used. The hydrogen atoms are randomly inserted into octahedral and tetrahedral sites. The time step was chosen to be 0.5 fs to include the hydrogen vibrational motions. All the samples are adequately deformed from 0% to 16% strain in z direction to cover both the elastic and plastic regions. Periodic boundary conditions are applied in all x, y and z directions. The Nose Hoover thermostat and barostat[110] are applied to control the temperature and pressure. NPT ensemble is applied. Thermal dynamical data are recorded each fs. Trajectories data are recorded each 10 fs for analysis. The initial kinetic energy of the system, which is correlated with temperature of 1K, was given to the system by Gaussian distribution. Then we increased the temperature from 1K to 700K in 7 cycles. For each cycle, temperature was first increased by 100K within 10 ps followed by a 20 ps relaxation run to equilibrate the systems. Then we sampled the system by extracting the thermal and trajectory data for 100 ps. This kind of 10 ps changing, 20 ps relaxing, and 100 ps sampling scheme will be used in all the simulations in this paper to ensure the systems are close to equilibrium states when we measure the properties. For sampling cycle, we will sample 10 time frames, once every 10 ps, for calculating the vacancy concentration by using "fill-in" method proposed by Suzhi et al[51].

5.3 Vacancy Concentrations of Equilibrium PdH Systems

For many chemical processes, such as hydrogen purification, membranes made by Pd and its alloys are yet the most advanced catalyst. The superior dissociative properties

of Pd can facilitate hydrogen absorption processes.[119] The working temperature is normally set to be above the critical threshold temperature where the miscibility gap no longer exist. It was believed that at elevated temperature, hydrogen embrittlement can be eliminated. Thus, we set the temperature range in this study to be from 300K to 700K. After the system was heat up and equilibrate, the vacancy concentration of pure Pd, $PdH_{0.01}$, $PdH_{0.02}$, $PdH_{0.04}$, $PdH_{0.06}$ and $PdH_{0.1}$. In pure metal, the vacancy concentration is following the Boltzmann distribution, as shown in equation 5.1.

$$C_{Va} = \frac{N_{Va}}{N_{Pd}} = \exp(-\frac{Q_{Va}}{k_B T}) \tag{5.1}$$

Where N_{Va} is the number of vacancy, N_{Pd} is the number of total lattice atoms, Q_{Va} is the vacancy formation energy for the system. According to literature, the Q_{Va} is around 1.44 eV for pure palladium. However, when the data is fitted by linear regression to the equation 5.1, we obtained Q_{Va} is 0.3445 eV, as shown in Fig. 5.1a, which is plotted in a form as equation 5.2.

$$-\ln(C_{Va}) = \frac{Q_{Va}(C_H)}{k_B T} - f(C_H) \tag{5.2}$$

The additional term f, which is a function of hydrogen concentration is added into the equation 5.2. The vacancy concentrations at 300K are too low to be correctly sampled, so that is not included in Fig. 5.1a. Here we consider both the activation energy and the additional constant term $f(C_H)$ as functions of hydrogen concentration, shown in Table 5.1. Also, the relative value of $f(C_H)$, which is the values of $f(C_H)$ subtracted by the $f(C_H=0)$, is also listed at the bottom of the Table 5.1, marked asΔf. Thus, we can quantitatively determine that the concentration of vacancy is not sorely depend on the vacancy formation energy when hydrogen is included. It was implied that the Q_{Va} is the dominating at low temperature. And $f(C_H)$ will be more critical at high temperature.

Table 5.1 Vacancy formation energy and the constant term as a function of hydrogen concentration.

C_H	0	0.01	0.06	0.1
Q_{va}	0.344523	0.341245	0.321376	0.31411
f	2.38948	2.51638	2.6094	2.85393
Δf	0	0.127	0.22	0.46445

To verify the EAM potential, a molecular static calculation of the relaxed vacancy formation energy was carried out in an 8x8x8 supercell of palladium at 0K and the value is 1.25 eV, which is much closer to the value of experimental value of ~1.6 eV.[120] To exam the influence of ensembles in the molecular dynamics simulation, the heating process is repeated by applying NVT ensemble to increase the temperature, and NPH ensemble to relax and sample data. In this way, the particle trajectories are closer to the unbiased microcanonical ensemble. By comparing the vacancy concentrations of systems in NPT scheme and NPH+NVT scheme in Fig. 5.1a and Fig. 5.1b, the influence of ensembles is observed to be minimal.

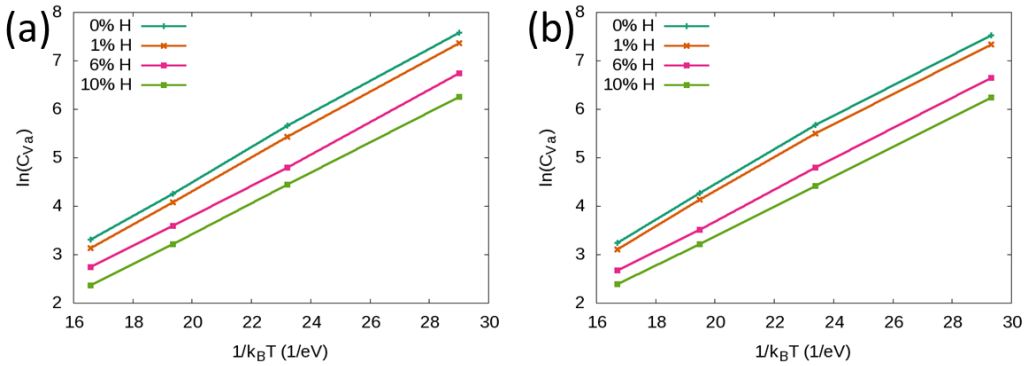

Figure 5.1 Effect of hydrogen to the vacancy concentration of the equilibrated systems at temperatures from 300K to 700K with (a) NPT and (b) NPH+NVT ensembles.

5.4 Influence of Mechanical Deformation to Vacancy Concentrations

The influence of plastic deformation at high strain rate to the vacancy concentration are well studied. Vacancies can be induced by the nonconservative motion of conventional jogs on screw dislocations at low temperature, whereas thermal jogs takeover at high temperature.[121] When hydrogen was brought in, the VHCs are stable and a linear relationship between strain and vacancy concentration was obtained by Suzhi et al.[51] in FeH solid solution system. However, the temperature effects to the vacancy concentration during deformation, which is crucial for PdH system, is also not explored so far by molecular dynamics.

On the other hand, the difficulties to accurately characterize and statistically analyze the vacancy concentrations are rigorous and two methods will be discussed and compared. The first one is Wigner-Seitz method, which is based on an “atom to atom” comparison between the defected lattice and a corresponding perfect lattice. But it requires that there are no dislocations, grain boundaries, or other 2D/3D defects in the system. The second method is “virtual atoms fill-in” method[51], which is based on the coordination numbers of the matrix atoms, can evaluate vacancy concentration when system is under

plastic deformations. And it is selected for this work since large mechanical deformation is applied.

One of the concern is the reliability of the "fill-in" method when system is approaching its elastic limit since the method is based on counting nearest neighbors. The threshold length for detecting nearest number is the mid-point between length of first nearest neighbor and second nearest neighbor which is 0.85355. It indicates that the first nearest bond can be stretched by 20.71%. This is far from the elastic limit for palladium metal, which is around 10% in <100> direction at 300K. So the anisotropic elastic strain should not significantly bias the vacancy formation energy. The thermal vibrations of the Pd atoms and the distortions caused by hydrogen atoms is the main contributors to the vacancy concentrations. Another issue is that, the dynamically calculated vacancy formation energy for pure palladium is 0.344523 eV, which is severely deviated. Also the melting point of the systems are underestimated by around 400K. These three effects will lead to the over-estimation of vacancy concentrations.

To eliminate the influence of over-estimations generated during deformation, we applied "error cancelation" method, which is widely used in the calculations in transition state theory, in the elastic portion of the deformation. Here, we first calculate the vacancy concentration as a function of strain, temperature, and hydrogen concentrations. (0% 1% and 10% hydrogen concentration cases are calculated) Then the 1% and 10% results are subtracted by the 0% results, so only the influences of hydrogen inclusion are left. The results are shown in Fig. 5.2 and Fig. 5.3 for the case of 1%-0% and 10%-0%, respectively. The subfigures (a) and (b) are for tension and compression deformations. There is no tensile/compressive asymmetry observed. For $PdH_{0.01}$ system, the influence of hydrogen inclusion is buried by the fluctuation of errors before 6% tensile strain and 5 % compressive strain. For the $PdH_{0.1}$ system, however, the influence of hydrogen is obvious all the way through the whole elastic deformation processes. For both samples, the higher the temperature, the larger the enhancement of vacancy crowding. This raw was well followed from 300K to 600K. But vacancy concentrations at 700K have shown irregular distortions. One of the possible explanation is that the high temperature has activated the

annihilation/curing mechanisms of vacancies, causing the droppings of the vacancy concentrations at 700K. Here, a linear model is introduced to explain the trends, as shown in equation 5.3[121]

$$C_{Va} = K\varepsilon + C_0 \tag{5.3}$$

where ε is strain, C_0 is the zero-strain concentration at specific temperature and hydrogen concentration. K is a function of stress (σ), as shown in equation 5.4.

$$K(\sigma) = \chi\Omega_0\sigma / Q_{Va} \tag{5.4}$$

in which χ is a dimensionless constant, Ω_0 is the atomic volume. By substituting the equation 5.2 and 5.4 into the equation 5.3, we obtained the full expression of vacancy concentration as equation 5.5.

$$C_{Va} = \chi\Omega_0\sigma\varepsilon / Q_{Va} + \exp[-\frac{Q_{Va}}{k_B T} + f(C_H)] \tag{5.5}$$

Through the equation we noticed that the first term on the right-hand side of the equation 5.5 determines mechanical deformations, whereas the second term controls the influence of thermal activation and hydrogen inclusion. The influence of hydrogen is not obvious in $PdH_{0.01}$ sample. The impact of hydrogen is getting stronger when the hydrogen concentration is in around 10%. In $PdH_{0.1}$ sample, lattice constant is about 0.4 Å larger than pure Pd sample. If lattice constant is expanded by 10%, Ω_0 will increase by 33.1%. Q_{Va} is decreasing when hydrogen atoms are included, as shown in Table 5.1. Thus, the trends in Fig. 5.3 are well explained.

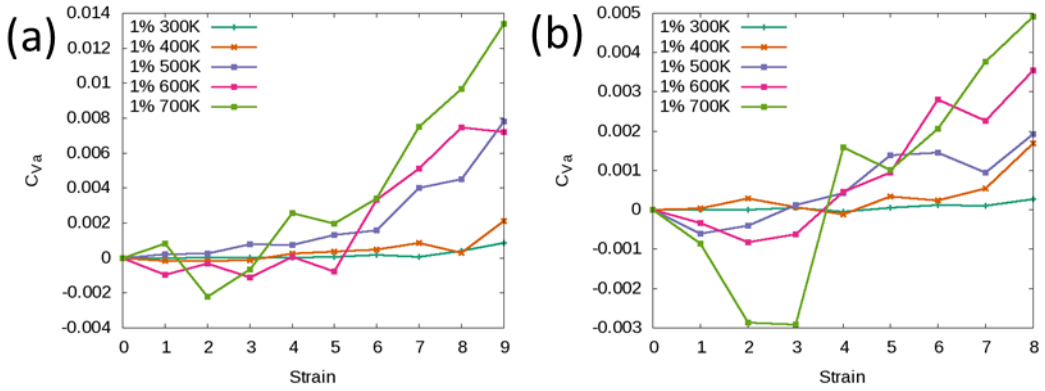

Figure 5.2 The intrinsic increment of vacancy concentration (i.e. $C_{Va}(PdH_{0.01})$-$C_{Va}(Pd)$) due to the inclusion of hydrogen atoms in $PdH_{0.01}$ system as a function of strain and temperature, (a) in tension, (b) in compression.

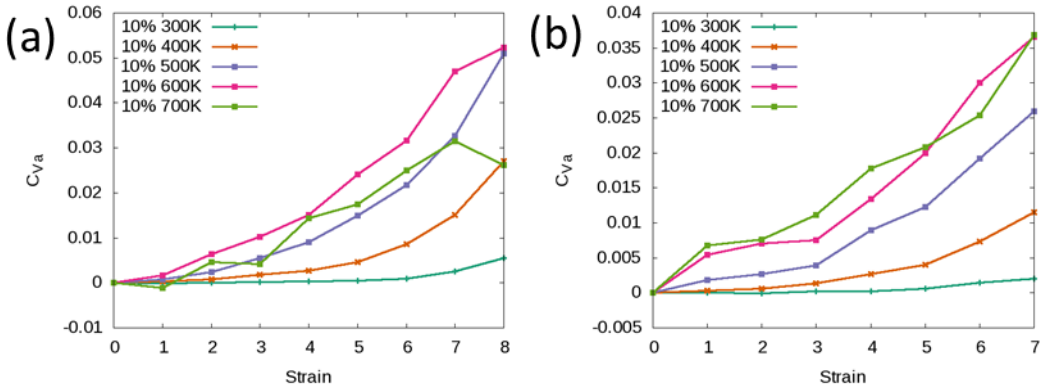

Figure 5.3 The intrinsic increment of vacancy concentration (i.e. $C_{Va}(PdH_{0.1})$-$C_{Va}(Pd)$) due to the inclusion of hydrogen atoms in $PdH_{0.1}$ system as a function of strain and temperature, (a) in tension, (b) in compression.

During the elastic deformation, vacancy concentration is a parabolic function of strain. It will become a linear function of strain when plastic deformation starts and the flow stress is stable. Also, work hardening can increase the amount of vacancies.

5.5 Conclusion

In conclusion, molecular dynamics calculations of vacancy concentrations as a function of uni-axial deformation, temperature, hydrogen concentrations in PdH system are conducted. Influence of hydrogen to equilibrium structures at different temperatures are qualitatively analyzed, a modified model is applied based on Boltzmann distribution to help explain the results. The vacancy formation energy is the dominating at low temperature, whereas the additional function $f(C_H)$ will be more critical at high temperature. The behaviors of vacancy concentrations during mechanical deformations are well explained by a linear model. Parabolic behaviors are observed during elastic deformations. The influence of hydrogen is minimal in $PdH_{0.01}$ sample, and becomes stronger in $PdH_{0.1}$ sample. The role of vacancy concentration is critical for the understanding of hydrogen embrittlement. The interaction of dislocations of vacancy clusters and the formation of nanovoids in front of crack-tips are promising for explaining the quasi-cleavage behaviors which have a combination of plastic and brittle characteristics.

6. NANOINDENTATION OF COHERENT TWIN BOUNDARY

6.1 Overview

Nano-indentation[122] has long been recognized as a well-proved, widely used mechanical testing method, which can offer rich information about the mechanical properties of the materials[122]. However, to carry out such a in-situ nanoindentation experiment with hydrogen loaded samples is difficult because an environmental chamber filled with hydrogen gas at certain pressure and certain temperature is needed.

On the other side, hydrogen embrittlement[45] is still a critical issue which is neither completely solved nor adequately well known[10, 11, 43, 123]. The complex hydrogen behaviors under stresses are initiated from nanoscales, which have raised tremendous challenges for experimental studies[124-127]. To fully understand the hydrogen effects on dislocations nucleation, propagation, and the correlated mechanical stabilities behaviors, many studies have been done and theories have been established[31, 32, 128-130]. The behaviors of dislocations interaction with hydrogen atoms[35, 81-86, 131], vacancies[5], and hydrogen-vacancies complexes[51] have drawn great interests. Interface interactions with dislocations in nano-twin[87-89] and nano-crystalline[132-134] metals are also explored by many groups. Although nano-crystalline metals have superior mechanical properties, they are instable in mechanical, thermal and chemical properties. On the other hand, nano-twin metallic materials, which have been proven to have superior strength, toughness and thermal stabilities[87, 135], have so far rarely been tested as a candidate material under stress-corrosion cracking environments[136]. In this work, we used molecular statics and molecular dynamics simulation methods to study the mechanical behaviors of nano-twined hydrogen palladium system. Simulated nano-indentation[79, 80, 137-142] were carried out to give an in-depth investigation of the nano-mechanical interactions between hydrogen interstitials, dislocations, twin boundaries, and mechanical deformations.

6.2 Simulation Method

Classical molecular statics (MS) and molecular dynamics (MD) methods, implemented by Large-scale Atomic/Molecular Massively Parallel Simulator (LAMMPS)[102] were used to simulate PdH system. The potential we used is an Embedded Atom Method (EAM) potential[99] developed by X.W. Zhou et al.[101] The total energy in EAM is in a from below.

$$E = F(\rho_i) + \frac{1}{2}\sum_{i \neq j} \varphi(r_{ij}) \tag{3.7}$$

in which F is the embedded energy functional, and φ is the pair-wise terms.

It was proved that this potential can successfully predict the phase stabilities, hydrogen diffusion paths, and mechanical properties of the PdH system. In this work, we studied the mechanical behaviors of the Σ3<111> symmetric tilt grain boundary (STGB), i.e. coherent twin boundary (CTB). At the beginning, a two-step molecular statics minimizations with Complex Conjugate method were used to relax the structures[143]. Energy tolerance was 10^{-15} eV and force tolerance was 10^{-15} eV/Å. In the first step, the simulation box was fixed, only the atoms could be relaxed. In the second step, the box was kept as tetragonal but could be relaxed in the normal direction of CTB. In order to fully understand how hydrogen reacts with the material in the indentation processes, four different indentation schemes were designed and implemented. They revealed the interactions between twin boundary, hydrogen atoms, and lattice defects. As demonstrated in Fig. 6.1, a spherical indenter with a radius of 50 Å is made by carbon atoms in diamond structure. It is indented at the two locations, which are the grain center between two grain boundaries and right at the CTB. The indent rate was set to be 89 m/s, which was in the range of typical applied rates for similar researches, i.e. 10m/s to 100m/s. A pure Pd sample and a $PdH_{0.1}$ sample were used to distinguish the effects of hydrogen inclusion. The indenter was kept at 0K with infinite mass. The interaction between the indenter and PdH were presented by Morse potential and obtained from literature.[144]

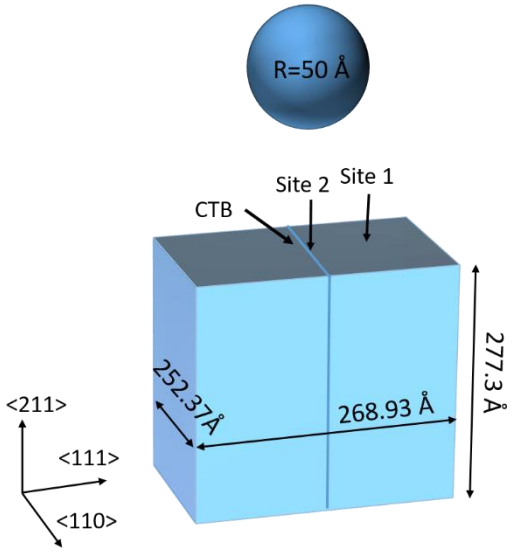

Figure 6.1 Schematics of the indentation model. The dimensions are for the pure Pd sample.

After molecular statics minimizations, random velocities which equivalent to 1 K were given to the atoms under Gaussian distribution. The pure Pd sample were then heat up from 1K to 10K by Langevine thermostat[145] under NVT ensemble in 20 ps. After a series of relaxation, most of the acoustic waves, which have direct influences on the results of indentation simulations, were eliminated. Hydrogen atoms are distributed preferentially at grain boundary and open surfaces. During the indentation, NVE ensemble is used with temperature rescaling when temperature is off the setting temperature by 10K.

6.3 Force Displacement Analysis

The force-displacement (*P-h*) curve of the pure Pd sample with indenter at the grain, i.e. sample [1], is presented in Fig. 6.2 (a), where there are several drops and fluctuations, corresponding to various defects interactions. The segments of black lines are manually added to help identify the fluctuations. Post-analysis and visualization are mostly done by Open Visualization Tool (OVITO).[146] To clarify the indentation process and defects movements, microstructure evolutions are presented by using Common

Neighbor Analysis (CNA) method, from points A through H in Fig. 6.2 (b), where FCC Pd atoms and the twin boundaries are removed for clarity. The red particles are representing HCP Pd atoms, whereas the grey particles are representing Pd atoms with unidentified crystal structures. The hydrogen and carbon atoms are removed for clarity. Dislocation Extraction Analysis (DXA) method is also used and presented in Fig. 6.2 (c) for showing the actual dislocation activities[146], among which the green dislocation sections are 1/6<112> Shockley partial dislocations (SPDs). The blue, purple, and yellow dislocation sections are corresponding to the 1/2<110> perfect dislocations, 1/6<110> stair-rod partial dislocations, and 1/3<001> Hirth partial dislocations, respectively. The capital letters A through H are used to correspond *P-h* curve with the actual microstructure evolution visualized by CAN and DXA.

6.3.1 Pure Pd Sample with Indenter at the Grain, Sample [1]

At elastic region, the *P-h* curve is parabolic. After system goes into the plastic region, at Point A, as shown in Fig. 6.2 (c), three Shockley partial dislocations (SPDs) with the three-fold symmetry emerged beneath the contact surface between the sample and the indenter. As indention continues, the upper dislocation source, labelled as α, serve as the dislocation nucleation site. The nucleated dislocations then evolve and propagate along the <110> directions highlighted by the dash lines in Fig. 6.2 (b). The other dislocation sources labelled as β and γ are suppressed by dislocations from site α at the beginning stage. However, prismatic loops always detach from the dislocation networks at β and γ sites around the indent surface. At point B of the *P-h* curve, where h=7.1 Å, fluctuations indicate the nucleation of new SPDs and formation of stacking faults. The corresponding dislocations morphology are shown in Fig. 6.3(b) and Fig. 6.4 (b) from two perspectives, in which the first prismatic loop is formed and the second prismatic loop is not formed yet. But its prerequisite SPD has nucleated. As the indentation process goes on, the second prismatic loop is formed shortly afterwards, at h=8.9 Å (point C). Both prismatic loops are going to propagate into the lattice along the trajectory before hitting any obstacles. The growth, propagation and detachment processes are well studied[141].

While the first pair of prismatic loops are propagating and adequate spaces under the indenter are available, the second pair of prismatic loops are formed at h=12.5 Å (point D). The full detachment processes are shown at point E-H, from h=16.5 Å to h=25.0 Å. Under the geometric confinement of the twin boundaries, the prismatic loops are propagating in directions parallel to the twin boundaries. The prismatic loops detached one after the other. The label sequence for the dislocations is identical to the sequence of the nucleation events, which is equivalent to the sequence of loops formation and dislocation detachments.

The sizes of first pair of prismatic loops are smaller than those of the second pair. It is indicated that the size of the prismatic loops is proportional to the contact surface between the indenter and sample. As the contact surface becomes larger, more volumetric deformations are induced. Larger loops can transfer larger deformations in the lattices. This is demonstrated in the work done by M. Wen et al.[80]. When prismatic loops reached an open surface, diamond shaped sinks formed on the surface. The amount of deformation is proportional to the cross-sectional area of the prismatic loop. Also, each side of the first pair of loops is parallel to the corresponding side of the second pair of loops. So, there will be similar diamond pattern on the open surface when more loops are generated.

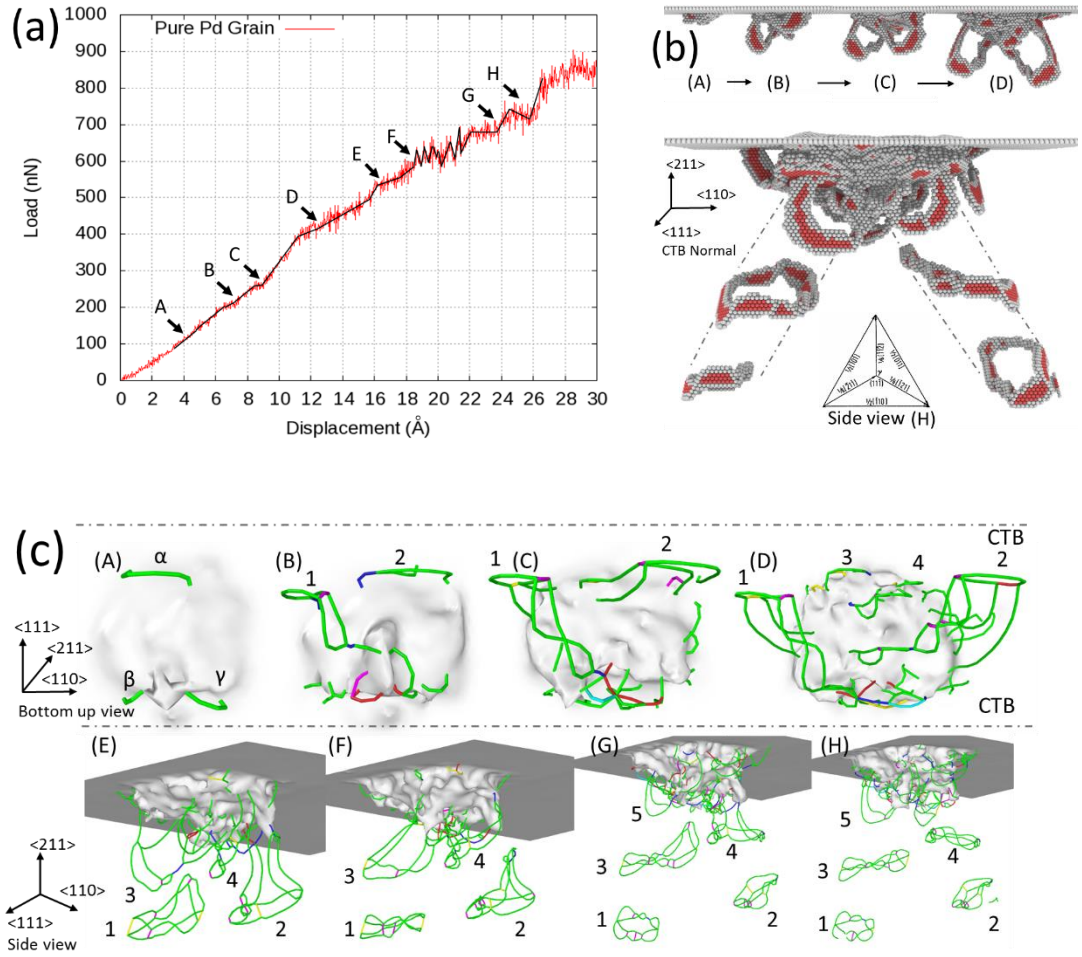

Figure 6.2 (a) Force-displacement curves of sample [1], the pure Pd sample indented at the grain, The points and displacements have a relationship as follow: (A) h=4.0 Å, (B) h=7.1 Å, (C) h=8.9 Å, (D) h=12.5 Å, (E) h=16.5 Å, (F) h=18.3 Å, (G) h=23.6 Å, (H) h=25.0 Å. (b) dislocation evolution using Common Neighbor Analysis (CNA) as a function of indent depth. The trajectories of the prismatic loops are shown as dash lines. (c) Dislocations evolution using Dislocation Extraction Analysis (DXA).

6.3.2 $PdH_{0.1}$ Sample with Indenter at the Grain, Sample [2]

The *P-h* curve of the $PdH_{0.1}$ sample with indenter at the grain, i.e. sample [2], is presented in Fig. 6.3(a), in which fluctuations are more severe than that in sample [1], indicating stronger defects interactions. The inclusion of hydrogen thus decreased the

mechanical stabilities of the crystal. At h=4.9 Å (point A), the three SPDs are formed and three dislocation nucleation sites are labelled as α, β and γ. The SPD 1 has already formed half of the prismatic shape from site α, at where SPD 2 has just nucleated. At h=6.2 Å, loop 1 has taken the lead and grown further into the crystal, SPD 2 has formed into loop 2 and ready to propagate after loop 1, but in different <110> directions. However, as indenter approaches h=10.3 Å, the loop 1 has multiple intersections with other dislocations and multiple stair-rod dislocation sections are formed, as shown in Fig. 6.3(c).

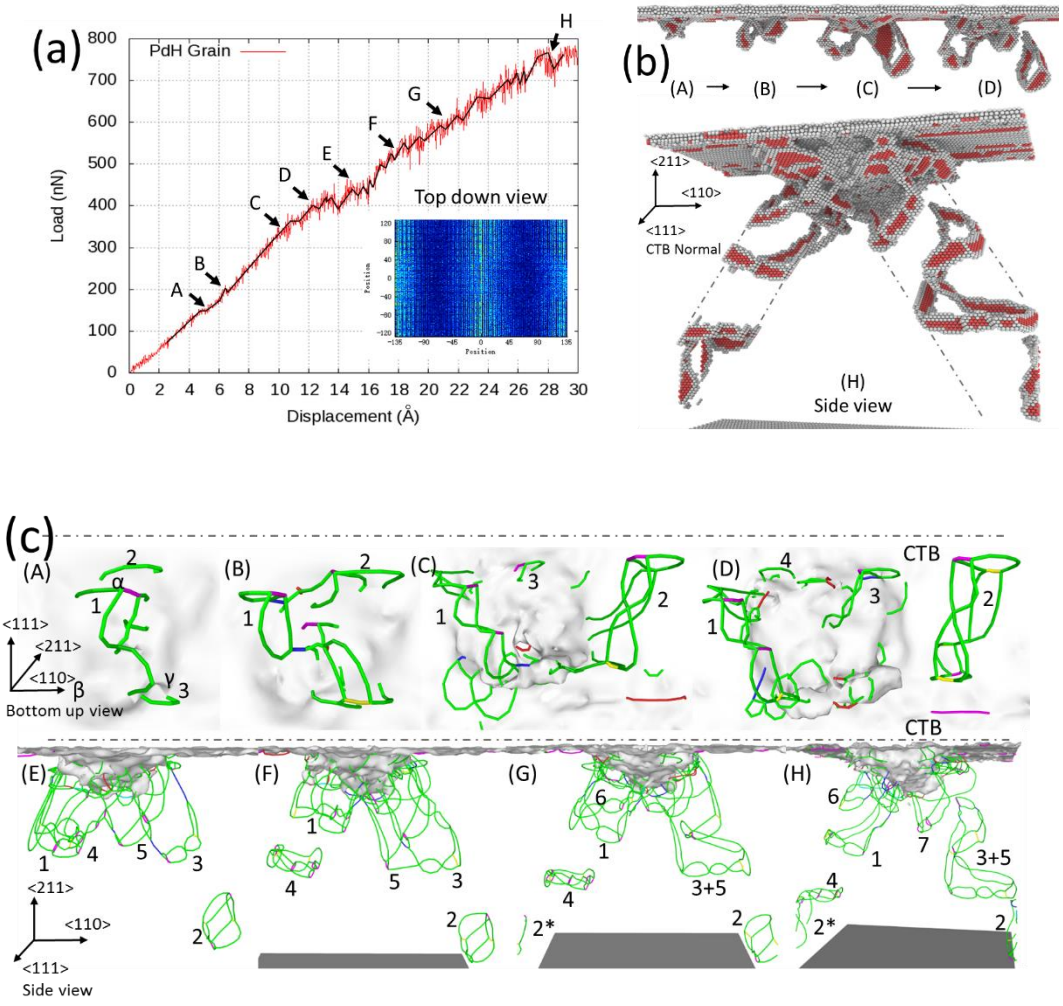

Figure 6.3 (a) Force-displacement curves of sample [2], the PdH0.1 sample indented at the grain, The points and displacements have a relationship as follow: (A) h=4.9 Å, (B)

h=6.2 Å, (C) h=10.3 Å, (D) h=12.0 Å, (E) h=14.7 Å, (F) h=17.8 Å, (G) h=21.0 Å, (H) h=28.1 Å. (b) dislocation evolution using Common Neighbor Analysis (CNA) as a function of indent depth. The trajectories of the prismatic loops are shown as dash lines. (c) Dislocations evolution using Dislocation Extraction Analysis (DXA).

These events changed the morphology and decreased the mobility of the loop 1. As consequence, loop 2 surpassed loop 1, detached from the dislocation source γ, and propagate further into the crystal. This event of loop detachment happened at h=12.0 Å (point D). Meanwhile, loop 3 is formed and SPD 4 is nucleated. At h=14.7 Å (point E), while the loop 2 has propagated into the crystal deeply. Loop 3 is entangled with loop5 and loop 1 is entangled with loop 4. At h=17.8 Å (Point F), loop 4 has overtaken loop 1 and detached from the dislocation networks while loop 1 is slightly bounced back into the dislocation network like a spring. Entanglement leads to severe fluctuations in the *P-h* curves from point D to point G, i.e. h=12.0 Å to h=21.0 Å. At h=28.1 Å. The loop 3 and 5 are merged into a double prismatic loop. With the assist of hydrogen, dislocation interactions are more active and frequent in sample [2] than sample [1].

6.3.3 Pure Pd Sample with Indenter at the Grain Boundary, Sample [3]

The *P-h* curve of the pure Pd sample with the indenter at the grain boundary, i.e. sample [3], is presented in Fig. 6.4(a). At h=6.2 Å, three dislocations are formed and labeled in Fig 6.4(c). Dislocations 4 and a “v-shaped” dislocation 5, defined as side growing dislocations (SGDs), are nucleated. SGDs are growing into <110> directions which are almost normal to the twin boundaries. Dislocations in sample [1] are mostly vertically growing dislocations (VGDs), growing vertically to the indent plane. At point C, where h=11.1 Å, SGD 5 merged with dislocation 1. The dislocation morphology on the two sides of the CTB has central symmetry along the indenter center in Fig. 6.4(c). At h=12.5 Å (point D), the prismatic loop 2 crossed the CTB and then detached from the site 4. Meanwhile, dislocations 3 and 6 has formed a complicated dislocation network. When the prismatic loop 2 is detached from the subsurface at h=14.7 Å (Point E), the prismatic loop 1 is struggling in crossing the CTB and moving forward. When h=18.3 Å (Point F),

prismatic loop 1 has crossed the CTB and linked with the successive loop 3. The entangled VGD and SGD have formed mixed dislocations and are also labelled as 6 and 8. The second prismatic loop is detached at Point G, when h =22.7 Å. At last, where h=25 Å, complicated dislocation networks are formed right beneath the indent surface, corresponding to the strain hardening right after point H in the *P-h* curve.

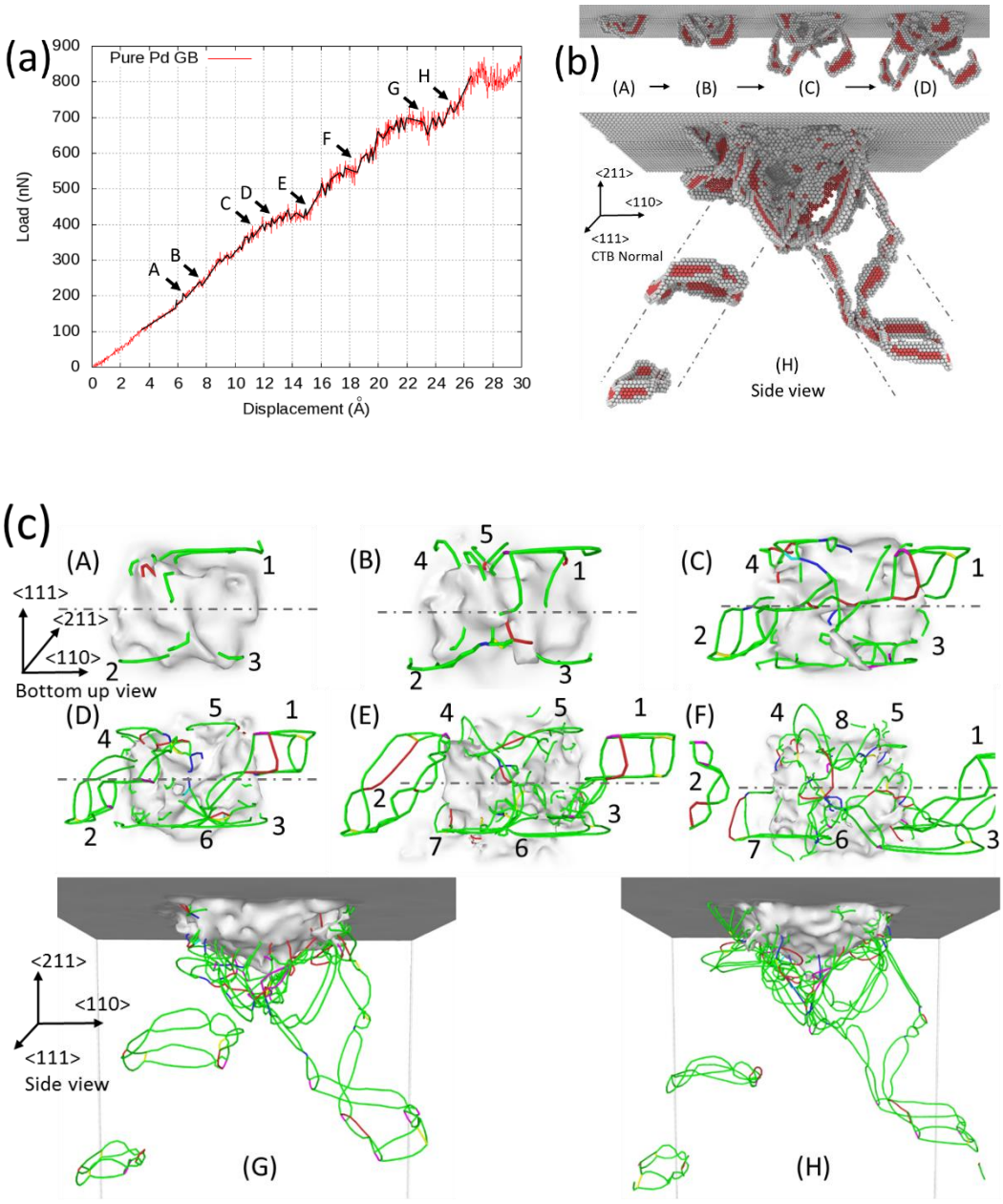

Figure 6.4 (a) Force-displacement curves of sample [3], the pure Pd sample indented at the grain boundary. The points and displacements have a relationship as follow: (A) h=6.2 Å, (B) h=7.6 Å, (C) h=11.1 Å, (D) h=12.5 Å, (E) h=14.7 Å, (F) h=18.3 Å, (G) h=22.7 Å, (H) h=25 Å. (b) dislocation evolution using Common Neighbor Analysis (CNA) as a function of indent depth. The trajectories of the prismatic loops are shown as dash lines. (c) Dislocations evolution using Dislocation Extraction Analysis (DXA).

6.3.4 $PdH_{0.1}$ Sample with Indenter at the Grain Boundary, Sample [4]

Sample [4] has unique properties compare to the other three samples.

Prismatic loops in sample [3] are formed and propagating in a way that like those in sample [1] and [2]. The formation of double prismatic loop is observed in both sample [2] and sample [3]. Sample [4] has unique defect morphologies compare to the previous three samples mainly because of the aggregation of hydrogen atoms at the grain boundary. The *P-h* curve (Fig. 6.5(a)) shows large vibrations after point E. As early as h=4 Å, there are yielding behaviors shown in the sample. From h=4 Å to 6.7Å, there are dislocations nucleated but then quickly disappeared. At h=6.7 Å (Point A), first stable SGD is formed and labeled as dislocation 1. On the other side of the CTB, the second SGD is nucleated. From point A to point B, the slope of the *P-h* curve is steep, indicating the formation and propagation of SGDs are energy demanding. The side view of the "v-shaped" SGD morphology of dislocation 1 and 2 are shown in the subfigure (c*) and Fig. 6.5(b). Dislocation 3 is then grown into SGD at h=14.7 Å (Fig. 6.5(c)-D). Dislocation 4 and 5 are then grown into VGDs, then formed prismatic loops (at h=16.5 Å). As dislocation 5 is grown faster with fewer dislocation entanglements, dislocation 4 and 6 are entangled with newly grown SGDs (at point F), so that their mobility is eliminated. At the final stage where h=25.9 Å, prismatic loop 5 is detached from the complicated dislocation network beneath the indenter. From point F to point G, although the fluctuations are violent compare to the earlier stage in the *P-h* curve, the overall slope of the curve is getting flatter, showing that the dislocation network is effectively transferring the strain and stresses into the sample, softening the surface.

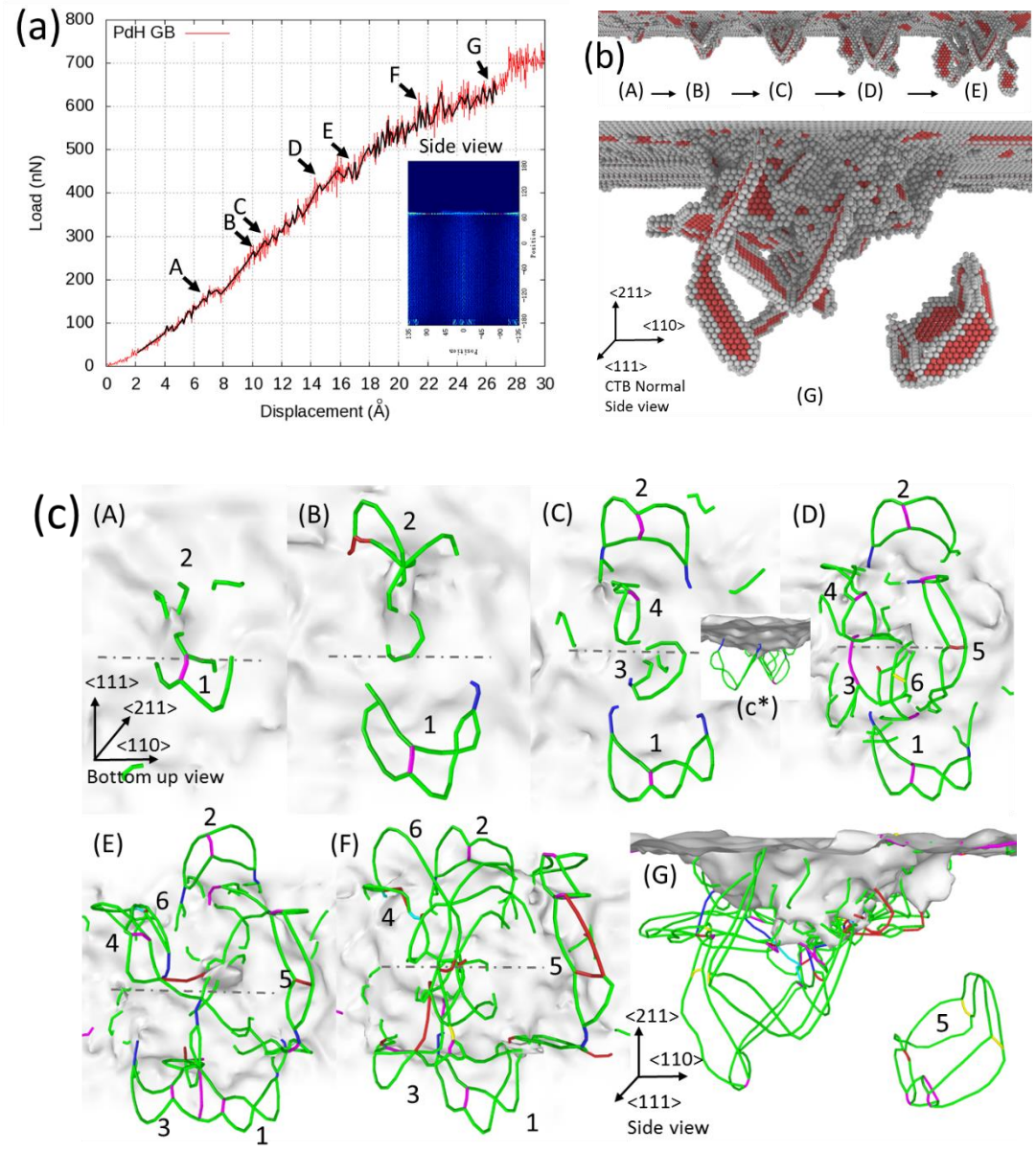

Figure 6.5 (a) Force-displacement curves of sample [4], the PdH0.1 sample indented at the grain boundary. The points and displacements have a relationship as follow: (A) h=6.7 Å, (B) h=9.4 Å, (C) h=11.1 Å, (D) h=14.7 Å, (E) h=16.5 Å, (F) h=18.7 Å, (G) h=25.9 Å. (C*) side view of h=11.1 Å. (b) dislocation evolution using Common Neighbor Analysis (CNA) as a function of indent depth. The trajectories of the prismatic loops are shown as dash lines. (c) Dislocations evolution using Dislocation Extraction Analysis (DXA).

6.4 Hydrogen-Defect Interaction

Hydrogen-Defect Interaction is important to fully understand the hydrogen embrittlement mechanisms.

6.4.1 Hydrogen Enhanced Dislocation Nucleation

When deformations are applied at the pure grain area, a dilute hydrogen inclusion can promote dislocation nucleation. The dislocation morphology of sample [1] at h=7.1 Å (Fig. 6.2(c)-B) is similar to that of sample [2] at h=6.2 Å (Figure 6.3(c)-B), whereas the morphology of sample [1] at h=12.5 Å (Fig. 6.2(c)-D) is almost identical to that of sample [2] at h=10.3 Å (Fig. 6.3(c)-C). This is indicating that the sample [2] needs smaller deformation than sample [1] for dislocation nucleation beneath the indent surface. At early stage of indentation, the dislocations are nucleated earlier in the PdH sample than in the pure Pd sample.

6.4.2 Hydrogen Enhanced Dislocation Mobility

The hydrogen distributions in the PdH sample is shown in Fig. 6.3(a), where lighter color is indicating higher concentration of hydrogen atoms. Hydrogen atoms are aggregating at the CTB and the indent surface. The concentration level of hydrogen in the grain area is comparatively low. With the presence of dilute hydrogen atoms in the grain area, dislocations can nucleate and propagate much quicker and with much smaller stresses. This is agreeable with the HELP mechanism[31]. For example, the displacements where first prismatic loop detached in sample [1] and [2] are 16.5 Å and 12.0 Å, respectively. Also, dislocations generate strain fields around them, so that the hydrogen atoms will be attracted to the areas which are under tension to neutralize the strains. With the ease of strain fields, dislocations are less interactive to each other. Thus, the mobility of the dislocations is further enhanced.

6.4.3 Hydrogen Enhanced Dislocation Entanglements

Although the intrinsic mobility of the dislocations is enhanced by the hydrogen atoms, the enhancement of dislocation nucleation and mobility also stimulated the growth of SGDs in the sample [2] and [4] compare to sample [1] and [3], causing dislocation entanglements between VGDs and SGDs. It will result in work hardening and stress concentrating in microscale. If the areas with high stresses are coincidentally located around crack tips, the stresses might induce crack propagation, thus endangers the mechanical stabilities. However, if the dislocation pile up happens in the perfect crystal, the risk is lower. This is partially the reason why the hydrogen cracking is unpredictable. The drastic changes of the microstructures and properties caused by hydrogen aggregation and the corresponding kinetic effects have made the problem more challenging.

By comparing the microstructure evolution of sample [1] and sample [2], the effect of dislocation entanglements is better illustrated. Sample [2] took the lead in dislocation propagation before h=12.0 Å compare to sample [1]. Its strong fertility induced SGDs nucleation at site β and entangle with prismatic loop 1 (Fig. 6.4(c)-D). SGDs decrease the motilities of the VGDs, causing the formation of a massive dislocation network. Jogs and kinks are formed on the dislocations. As consequence, the second prismatic loop detached from the dislocation network at h=18.3 Å in sample [1] and at h=17.8 Å in sample [2]. Thus, the advantages of the sample [2] in dislocation evolution has vanished because of the entanglement of dislocations.

6.4.4 Effect of Twin Boundary: Isolation, Strengthening and Hydrogen Aggregation

CTBs can act as a barrier for the isolation of stresses and dislocations, keep the neighboring crystal free of dislocation when it is under 30 Å indent depth, e.g. sample [1] and [2]. When a dislocation loop is attempting to cross a twin boundary, the high energy barriers making the process slow. When a prismatic loop is crossing a CTB, the friction is increased for dislocation gliding, causing work hardening. For instance, in sample [3], the loop 1 has struggled in crossing the CTB, which has given enough time for loop 3 to

develop itself (Fig. 6.4(c)-D), leading to the fusion of the two loops into a double prismatic loop structure, as shown in Fig. 6.4(c)-G.

Apart from sample [1-3], the unique behavior of sample [4] is due to the hydrogen aggregation at the CTB and the indent surface, which has changed the structure around them. But the crystal structure of Pd matrix around the CTB regions is remained as FCC before the indentation. Dislocations have low mobility at the hydrogen concentrated regions. The surface hydrogen atoms have roughened the surface, making heterogeneous dislocation nucleation easier. The level of entanglement between VGDs and SGDs has a relationship as sample [4] > sample [3] > sample [2] > sample [1]. VGDs are dominating in sample [1] and [2], and SGDs are rarely seen in these two samples. Both the extended dislocation propagation volumes (i.e. in sample [3] and [4], dislocations can nucleate and grow in two adjacent grains, where in sample [1] and [2], dislocations are grown in one isolated grain) and hydrogen inclusion have positive effects on the nucleation and growth of SGDs. However, the extended volumes are the dominating factor.

6.4.5 Statistics of Dislocations Lengths

We summarized the length for the 1/2<110> perfect dislocations, 1/6<112> Shockley partial dislocations (SPDs), 1/6<110> stair-rod partial, total dislocation length, and total number of segments of dislocations in Table [6.1-6.4] for sample [1-4], respectively. Data from different characteristic moments are summarized to compare with the corresponding dislocation morphologies. Hirth, Frank and other unidentified dislocations are disregarded as their values are either very low or unreliable. For sample [2] and [4] which contains 10% of H, there are around 200 Å Stair-rod dislocations pre-existed on the indent surface.

By comparing the data from sample [1] and [2], the conclusion are similar to what we found in the discussion section. At early stage of the indentation, where h < 10 Å, sample [2] has taken the lead in dislocation nucleation. When h=8 Å in sample [1], and h=5.5 Å in sample [2], their lengths for SPD are close. This indicates that the stress requirement for initial dislocation nucleation process is decreased with the inclusion of

hydrogen. The length of SPDs and total dislocations of sample [2] is 10-20% more than that of sample [1] when h>10 Å.

When compare sample [1] with sample [3], i.e. the difference caused by indentation sites, the phenomenon is very consistent along the whole indentation process. Sample [1], which dislocations are growing in an isolated layer of perfect crystal, has shorter lengths for SPD and total dislocation compare to sample [3]. Although the CTB and the dislocation multiplications of VGDs and SGDs in sample [3] has interfered the dislocation propagation processes, dislocations in sample [3] has two grains for growth and propagation whereas sample [1] and [2] only have dislocations grown in one grain. So at h=28 Å, length of SPD in sample [3] is 4264 Å, whereas in sample [1] is 3492 Å. Sample [4] has obviously overall lower values for dislocation lengths because of its unique structure.

Table 6.1 Length of different kinds of dislocations at different Indentation stages for pure Pd sample indented at the grain, i.e. sample [1].

Dis\Depth(Å)	4.0	7.1	8.9	12.5	16.5	18.3	23.6	25.0	28.1
Perfect	0	28.63	6.53	37.3	106.3	80.84	213.2	283.2	339.64
SPD	46.5	260	595.02	1107.9	1882.1	2045.4	3158	3492	3974.9
Stair-rod	0	17.7	21.28	38.44	38.23	65.15	203.6	211.1	187.02
Total length	46.5	327.2	691.02	1301.6	2118	2351.8	3961	4307	4898.6
Total segments	3	22	44	79	118	152	262	268	324

Table 6.2 Length of different kinds of dislocations at different Indentation stages for PdH0.1 sample indented at the grain, i.e. sample [2].

Dis\Depth(Å)	0.0	4.9	6.2	10.3	12.0	14.7	17.8	21.0	28.1
Perfect	0	0	13.26	14.15	27.08	56.02	78.13	164.28	278.03
SPD	51.84	247.92	447.11	947.76	1254.2	1990.3	2666.7	3250.2	4780.1
Stair-rod	189.8	178.21	184.22	217.33	268.4	326.34	255.8	335.6	342.14
Total length	252.7	454.04	695.6	1254.8	1652.2	2453.5	3163.5	3973.4	5838.9
Total segments	16	30	49	82	116	140	197	220	336

Table 6.3 Length of different kinds of dislocations at different Indentation stages for pure Pd sample indented at the grain boundary, i.e. sample [3].

Dis\Depth(Å)	6.2	7.6	11.1	12.5	14.7	18.3	22.7	25.0
Perfect	0	4.09	38.86	47.92	42.88	140.4	122.2	163.96
SPD	175.15	383.24	888.33	1302.1	1766.3	2542.3	3563.5	4263.9
Stair-rod	0	6.73	29.79	24.95	34.37	51.03	187.53	144.7
Total length	185.64	426.34	1092.3	1531.9	2020.7	3047.6	4381.5	4991.6
Total segments	9	28	76	87	132	195	265	290

Table 6.4 Length of different kinds of dislocations at different Indentation stages for PdH0.1 sample indented at the grain boundary, i.e. sample [4].

Dis\Depth(Å)	0	6.7	9.4	11.1	14.7	16.5	18.7	25.9
Perfect	0	0	10.72	37.22	44.03	86	46.87	100.4
SPD	57.92	191.93	377.79	544.14	863.4	1395.3	1671.4	2987.5
Stair-rod	207.25	170.4	179.1	202.89	243.3	241.6	243.1	304.5
Total length	265.17	394.7	606.18	787.26	1202.3	1800.2	2156.7	3964.5
Total segments	17	27	41	51	76	124	133	236

6.4.6 Hardness and Young's Modulus

The hardness and Young's modulus are calculated and the methods and results are presented in the supporting information section. In sample [4], the highly softened CTB has decreased the Young's modulus by over 30 GPa when compare with sample [3]. The hardness is also decreased by 3-4 GPa at the beginning stage of the indentation for sample [4]. Sample [1-3] have similar performance in terms of hardness and Young's modulus.

According to Hertz contact theory, the reduced hardness can be calculated by equation 6.1

$$P = \frac{4}{3} E R^{\frac{1}{2}} H^{\frac{3}{2}} \tag{6.1}$$

in which P, E, R, and H are the Load of indenter, Reduced modulus, indenter radius and indentation depth.

$$\frac{1}{E^*} = \frac{1-\nu_1^2}{E_1} + \frac{1-\nu_2^2}{E_2} \tag{6.2}$$

in which E^* is the reduced modulus, E1, E2 are the elastic moduli and v1, v2 are the Poisson's ratios associated with the indenter and the substrate surface.

The Young's modulus of the sample [1-4] are listed in Table 6.5. So the Young's modulus of sample [1] showing that our results are in well fit with experimental value of 120 GPa for pure Pd sample. The Poisson's ratio of the all the samples are assumed to be the experimental value of the Poisson's ratio of pure Pd, which is 0.39. The results showing that sample [1-3] have similar Young's modulus. The dilute hydrogen smeared in the grain area doesn't affect the Young's modulus effectively. However, sample [4] showing enormous softening effects when the indenter is approaching the CTB with aggregated hydrogen atoms. The young's modulus of sample [4] have 30 GPa lower than the rest samples.

Table 6.5 Young's modulus of sample [1-4] obtained from Hertz contact theory.

Sample [1] Pd_Grain	Sample[2] PdH_Grain	Sample[3] Pd_GB	Sample[4] PdH_GB
121.95 GPa	124.7 GPa	128.52 GPa	91.57 GPa

The hardness of the samples are calculated by the equation 6.3 and shown in Fig. 6.6.

$$H = P/(\pi(2R-h)h) \tag{6.3}$$

where H, P, R, and h are the hardness, Load of indenter, indenter radius and indentation depth.

In general, samples with hydrogen atoms are softer than pure Pd samples. However, samples [1-3] have similar Hardness curves compare to sample [4]. Again, the CTB-Hydrogen complex structure showing much lower hardness, especially at the beginning stage of the indentation.

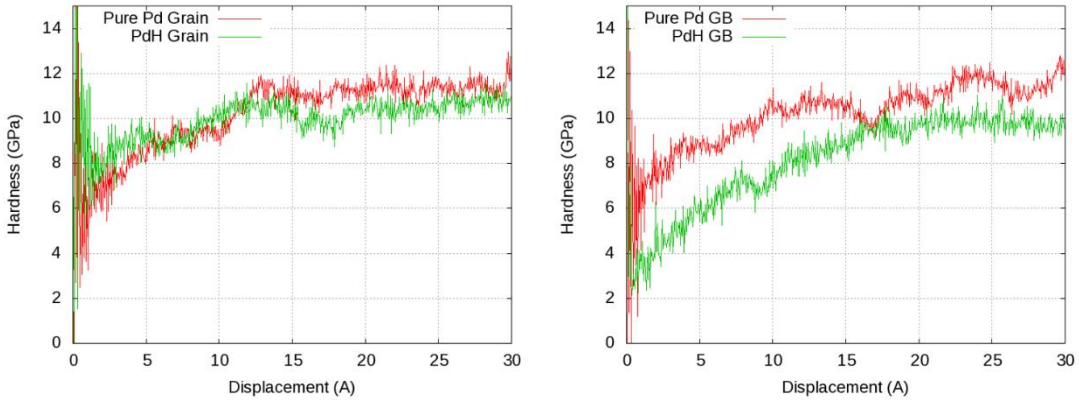

Figure 6.6 Hardness of sample [1-4] in unit of GPa during the indentation process.

6.5 Conclusion

Hydrogen palladium system with coherent twin boundary (CTB) structure is tested by simulated nano-indentation processes. Molecular statics and molecular dynamics techniques are used. There are four simulation schemes, including pure samples and $PdH_{0.1}$ samples which are indented at the grain center between two CTBs and right at the CTB, respectively. We conclude that

1. Diluted hydrogen atoms in the grain stimulates the dislocation nucleation processes and increased the mobility of dislocations. It also induced the growth of side grown dislocations, which will have dislocation entanglements with the vertical grown dislocations and slow down the overall dislocation propagation processes.

2. When a dislocation loop is trying to cross a twin boundary in pure Pd sample, its mobility will decrease and energy accumulations are needed before it can overcome the barrier. However, when a CTB is already crossed a dislocation loop and stayed in the center of the loop, its mobility is recovered.

3. The hydrogen aggregation at the twin boundary changed the morphology of dislocation evolution. The vertical grown dislocations are not favored to grow and glide in the H concentrated area near the CTB. As an alternative, side grown dislocations are expanded into the grain regions with lower hydrogen concentrations. Large amount of dislocation entanglements in sample [4] have made the dislocation propagation to be the slowest one in all four samples. The CTB is acting as a buffer area which can absorb a large amount of stresses.

7. NANOPILLAR PLASTICITY WITH HYDROGEN

7.1 Overview

Single crystal nanopillars have been attracting substantial attention due to its outstanding mechanical performance[47, 147], as well as their electrical[148, 149], magnetic[150] and catalytic properties[151]. It is the key component in nano-electro-mechanical-systems (NEMS)[152]. The growing abilities to characterize and operate nanopillars during deformation processes offer great potential to understand the microscopic plasticity and size dependence[153-158]. For example, compressive yield strengths are around 9 GPa for molybdenum nanopillars with different diameters[159, 160]. The observed large strength of the pillars is conjectured to be benefitted from their near defect-free structure[161]. Apparently, with limited internal volume, dislocations will propagate to and annihilate at the surface of the pillars shortly after their nucleation, with minimal probability for multiplication[162]. Due to this dislocation starvation phenomenon[163], work hardening in nanopillars is not as dominant as in polycrystalline materials[164]. To fully understand the plasticity of nanopillars, three factors will be introduced and discussed. First, due to the high surface to volume ratio, the surface formation energy[165] and corresponding surface stress are important. Second, generalized stacking fault energy (GSFE) was invented by Vitek[166] as a method to predict dislocation core structure, and Rice[167] used the GSFE curve in models of dislocation nucleation. In FCC metals, GSFE curve are typically computed along <112> direction on the 111 plane, which is the partial dislocation with Burgers vector 1/6<112>, according to dislocation theory[168]. Finally, Schmid factor[169, 170] is essential for the explanation of the orientation effects of the plasticity in nanopillars.

In metallic single crystal nanopillars, slip and twinning are two major plastic deformation mechanisms. The competition between deformation twinning and dislocation sliding is critical since each of them will lead to very different mechanical response and surface morphology[171] of the pillar. But it is strongly influenced by temperature[172], strain rate[48], crystal orientation[66], facet surfaces[173], activation volume of defects etc.

On the other hand, hydrogen embrittlement has been a long lasting metallurgical challenge[123]. The confusion comes from the unidentified microscale events of various defects and how they accumulate and cooperate to form the macroscopic embrittlement failures. These microscale to macroscale failure processes are influenced by extrinsic and intrinsic influences. Extrinsic influence includes temperature, strain rates, fracture modes, oxygen content[9] and chemical potential[1] of hydrogen etc. Intrinsic effects contain mechanical properties, chemical composition of alloys, phase polymorphism, spin influence for magnetic materials[82], crystal orientation[174], preexisting defects[175], diffusion of hydrogen atoms[107], geometries of parts etc. The change of all these factors hinders hydrogen embrittlement to be fully understood. It is proposed that one should try to eliminate the uncertainties down to a controllable level, then use the simplified models to study the hydrogen embrittlement.[44]

Here, a simplified model, single crystal pristine cylindrical palladium pillars with fixed geometry, strain rate and room temperature are studied under different orientations and with/without 10% of hydrogen inclusion. We are interested in heterogeneous nucleation of defects and their competition at the situation with free surfaces. Tensile deformation was employed instead of compression to avoid the bending and frictions[48]. The hydrogen influence on the generalized stacking fault energy is calculated and used to explain the competition between slip and twin. Results show that for [001] direction, full dislocations are the main plastic deformation mechanism. Full dislocations propagate to the free surface after their nucleation, leading to defect starvation and serrated stress strain curves. For [111] and [110] orientation, deformation twinning is the predominated defect. The substantial nucleation of partial dislocations released stress accumulations, leading to a smoother stress-strain response. Partial dislocations are propagating in [112] oriented pillars. Under the influence of hydrogen, deformation twins are nucleated in [112] orientated pillars. Hydrogen also facilitates the nucleation of partial dislocations in [001] pillar.

7.2 Simulation Method

In the simulations, perfect FCC single crystals with 10 nm radius and 60 nm length are shaped with axial direction pointing at [100], [110], [111] and [112] crystal directions. It is believed that the trend in deformation mechanisms in 10 nm radius will be valid for radius up to 50 nm.[176] Systems contained approximately 1.3 x 10^6 Pd atoms. The simulations were performed by implementing the molecular dynamics (MD) program LAMMPS[102] and embedded atom method (EAM)[99] potential for PdH system[101] was employed. Tensile deformations were carried out in NVT ensemble at 300 K with a time step of 1.0 x 10^{-15} s for pure Pd pillar, and 0.5 x 10^{-15} s for PdH pillar. The OVITO[146] software was used for visualizing the defect evolutions.

The perfect pillars were relaxed for 4 ns in vacuum to equilibrate the free surfaces. Then the uniaxial tension was applied along the axial directions of the pillars. This was done by elongating the simulation box in the axial direction so that the pillars were deformed uniformly before defect nucleation. The strain rate was set as 10^8/s[177]. During the deformation, an extra 2 nm layer were fixed at both the bottom and top layer of the pillars. The maximum strain values were set to about 20%. The trajectory and stress-strain relationship were recorded for further analysis.

7.3 Plastic Deformation Mechanism for Pure Pd Samples

Fig. 7.1 shows the stress-strain curves of nanopillars with [001], [110], [111] and [112] directions, with and without 10 atomic percent of hydrogen. The orientation effects on yield stress and the plastic flows are obvious. For yield strength, pure Pd sample with [100] direction has the highest value of 6 GPa. For pure Pd sample in [110] direction, the yield stress is merely 3.5 GPa. For [111] and [112] oriented sample, the yield strength is around 4 GPa.

To better analyze the various plasticity responses observed in Fig. 7.1, the microstructure evolution during the tension was carefully examined. Fig. 7.2(a) shows the microstructural evolution of the [001] oriented pure Pd sample. Snapshots in Fig. 7.2(a)

A-E are related to the highlighted points (A-E) in the Fig. 7.1 a. In Fig. 7.2 and Fig. 7.3, the deformation processes are illustrated by the Common Neighbor Analysis (CNA)[178]. Atoms on perfect fcc lattice sites are set to be invisible. Atoms with hcp structure are shown in red, whereas atoms don't belong to any crystal category is shown in grey. All the pillars are split into half along the tensile direction and only half of the sample are shown.

From the snapshots in Fig. 7.2(a) A, stacking faults bounded by partial dislocations on four different [111] planes nucleated in Pd [001] sample almost simultaneously, which leads to the drop of stress. At stage A, only leading partials are nucleated. At later stage, after the nucleation of the trailing partials, more and more full dislocations are nucleated and intersect with each other, as shown in Fig 7.2(a) B, leading to a further drop of stress. After all the nucleated full dislocations propagated to surface, the interior of the pillar is remained as pristine, leading to the hardening caused by dislocation starvation. Also, the limited dislocation cross-slip and entanglement has a work hardening effect shown in the stress strain curve, leading to a serrated pattern. As shown in Fig. 7.2(a) D and Fig. 7.2(a) E. The drop of stress after point D and E are caused by new dislocation nucleation events. On the surface of the pillar, stages are formed and necking are initiated in the lower half of pillar.

Fig. 7.2(b) shows the microstructural development of the [110] oriented Pd pillar under tension. Snapshots in Fig. 7.2(b) A-E are related to the highlighted points (A-E) in the Fig. 7.1 (b). As shown in Fig. 7.2(b) A, leading partials of dislocations are nucleated after the first yielding. Unlike the [100] pure Pd sample, the tailing partial nucleation is not observed in the [110] sample. Once the leading partial reached the other end of the free surface, new leading partials are nucleated and grow into the pillar. The deformation twinning is predominating in the [110] sample. The constant and stable nucleation of partial dislocations leading to a stable and less serrated flow stress after yielding. From snapshot (B to E), two sets of deformation twinning are initiated and propagating into the middle of the pillar. The interior of the sample is very clean with minimum defects besides the twin boundaries, indicating that the deformation twinning can effectively dissipate the

deformation energy and annihilate (absorb) other defects, e.g. vacancies and dislocations. Due to twinning, the shape of the pillar is moderately twisted. Necking are observed at the lower end of the pillar.

Fig. 7.2(c) shows the microstructural development of the [111] oriented Pd pillar under tension. Snapshots in Fig. 7.2(c) A-E are related to the highlighted points (A-E) in the Fig. 7.1 (c). Dislocation are nucleated at the surface of pillar, as shown in Fig. 7.2(c) A. In [111] direction, twinning is the predominant mechanism, however, full dislocations are also active. In Fig. 7.2(c) B, the deformation twinning is nucleated, and twin grain is ready to grow. From point B to point E, the effect of full dislocation slip has resulted in necking at the bottom and mid-range of the pillar. Meanwhile, the twin boundaries are moving so that the twin grain is thickened, dissipating the deformation stresses. In Fig. 7.1(c), while the continuous nucleation of partial dislocation will move the twin boundary forward and offers a smooth stress strain curve, dislocation nucleation and interactions are inducing small fluctuations in to the mechanical response.

Fig. 7.2(d) shows the microstructural development of the [112] oriented Pd pillar under tension. Snapshots in Fig. 7.2(d) A-E are related to the highlighted points (A-E) in the Fig. 7.1 (d). Since dislocations nucleate separately on the (-11-1) and (1-1-1) slip planes and propagate immediately in the pillar. Parital dislocations are nucleated then propagate with less entanglement compare to [100] pure Pd pillar are observed from point B to point E. Besides, full dislocations are also observed. Comparing the stress strain curve of these two pillars, [112] oriented pillar shows less fluctuations in stress. However, both samples are governed by the dislocation starvation mechanism and no deformation twinning are observed for these two sample below 20% strain at 300K.

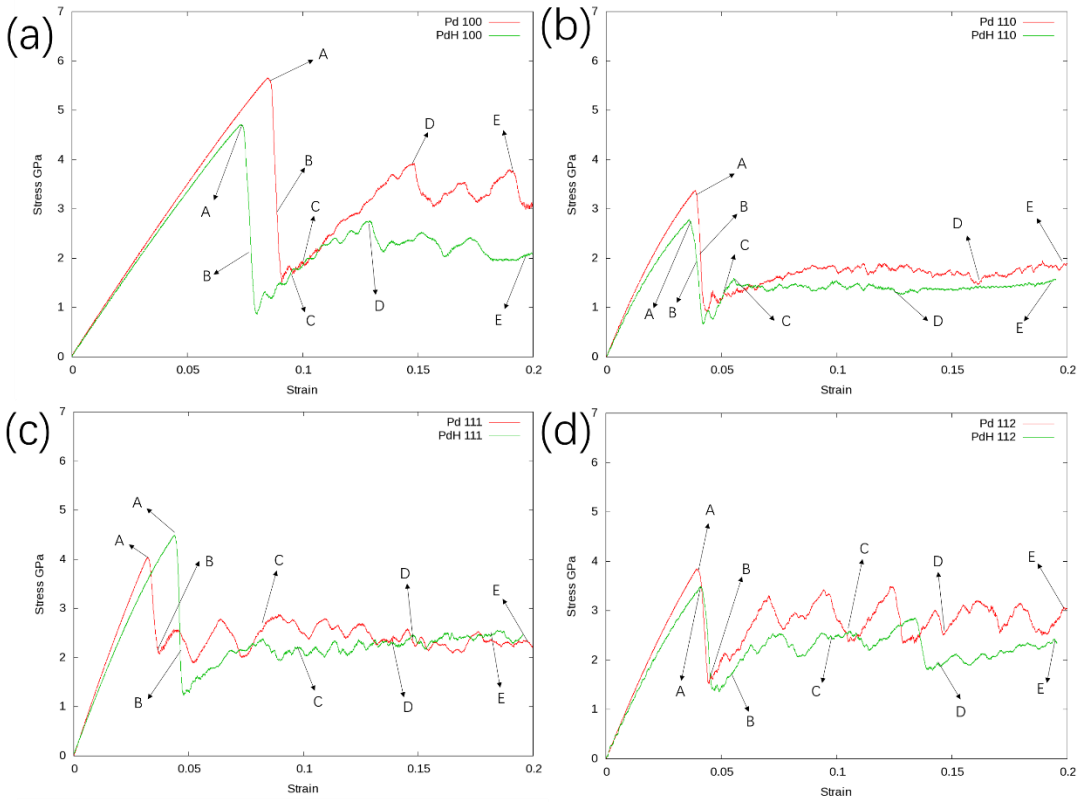

Figure 7.1 Stress-strain curves for nanopillars with various crystal orientations for pure Pd and PdH0.1 samples. (D=20nm, T=300K)

7.4 Hydrogen Influence on Nanopillars

Hydrogen embrittlement has a broad impact in metallurgy due to its ubiquitous availability. In any corrosion reaction scheme and any acid environment, hydrogen will be produced. It exceedingly high diffusivity makes it much worse than other impurities. To analyze the source of the embrittlement, various mechanisms are developed. However, they all make sense under their limited hypothesis. A general scheme is lacked so far. For example, hydrogen enhanced localized plasticity (HELP)[31] claimed that hydrogen inclusion can lower the dislocation nucleation energy and Peierls stress[167] for dislocation gliding, so that the localized plasticity is enhanced. On the other hand, hydrogen enhanced

decohesion (HEDE)[46] promotes that hydrogen will weaken the metallic bond between the atoms and induce premature lattice decohesion, lead to brittle failures. According to Adsorption Induced Dislocation Emission (AIDE)[45], the absorbed hydrogen might facilitate the nucleation and migration of dislocations at surfaces away from the crack tips. It also involves the nucleation and growth of nanovoids in front of the crack. Voids formation facilitates crack growth, also sharpen the crack-tip. However, most of these theories are developed for engineering materials with abundant pre-existed defects. For perfect single crystal nanosystems, the rules are not well defined yet. Here, systems with 10 atomic percent of hydrogen, i.e. the quantitative ratio between Pd and H is 10:1, are included. This is much higher than than the solubility of hydrogen in other FCC metals, e.g. Ni, Cu etc[179, 180]. This will be interesting, since under high tensile uniaxial, biaxial or hydrostatics stresses, the local solubility of hydrogen can be increased, leading to locally concentrated hydrogen content[181].

By comparing the stress strain curves in Fig. 7.1, in general, the $PdH_{0.1}$ samples in all directions show lower young's moduli, due to the smaller slopes in the stress strain curves, compared to their pure cases. Also, the yield stresses of $PdH_{0.1}$ samples are lower by 20% than the pure samples. However, there is an exception in [111] direction, which both the yield stress and yield strain of the hydrogenated sample are larger than the corresponding pure Pd sample. The flow stress in the $PdH_{0.1}$ samples are lower than those of the pure Pd samples. This is an indication that both slip and twinning are more mobile with hydrogen[80], leaving the system with less stress concentration. Hydrogen inclusion also stimulate the nucleation of partial dislocations and deformation twinning[49].

In [100] direction, with the inclusion of hydrogen, partial dislocations are nucleated in addition to the full dislocations, as shown in Fig. 7.3(a) A-E. Dislocation starvation is achieved, but with some paritial dislocations left in the pillar. From Fig 7.3(a) E, we can observe that the necking of the pillar is more obvious than the pure [100] sample, indicating that the local plasticity is enhanced and dislocations are more easily nucleate and propagate to the surface. This is revealed in stress-strain curves, with the fact that the flow stress of $PdH_{0.1}$ sample is lower and smoother.

For [110] direction, similar pattern is observed in both pure and $PdH_{0.1}$ samples. However, in the pure sample, two deformation twinning partials are activated, one at each end of the pillar. In the $PdH_{0.1}$ sample, as shown in Fig. 7.3(b) C, the similar two twinning partials are nucleated. However, under the influence of hydrogen, the upper partial became mobile and dissipated the energy before the lower partial is ready to move. In Fig. 7.3(b) D, the lower partial dislocation is annihilated, and the upper deformation twin controls transforming the deformation energy into reorientation of the crystal. Even with one set of partial dislocations, the $PdH_{0.1}$ sample has lower flow stress than the pure Pd sample, indicating that hydrogen can enhance the mobility of twin boundaries and the nucleation of partial dislocations. Meanwhile, twin boundaries are acting as sinks for dislocations and vacancies, as shown in Fig. 7.3(b) E. The flow stress is stable in the $PdH_{0.1}$ sample.

In [111] direction, the yield stress and yield strain for the $PdH_{0.1}$ sample is higher than the pure Pd sample, even though the young's modulus has decreased. Several set of samples with different diameters are tested under the same condition to verify this peculiar result. It might be caused by the imprecise description of general stacking fault energy landscape. After yielding, the flow stress in the $PdH_{0.1}$ sample is lower than the pure Pd sample. The pattern of defect evolutions is similar for both sample, i.e. the deformation twinning is predominant, full dislocations are exhausted. One interesting feature is that in the $PdH_{0.1}$ sample, there is a nanocrystal that is nucleated, as shown in Fig. 7.3(c) E. At the end of the deformation, the flow stress of $PdH_{0.1}$ sample is exceeding that of the pure sample.

In [112] direction, the yield stress of $PdH_{0.1}$ sample is lower than the pure Pd sample, whereas the yield strain is higher than the pure Pd sample. The deformation processes are illustrated in Fig. 7.3(d) A-E. After yielding, both samples show serrated flow stress. The deformation mechanism for both sample is governed by dislocation starvation. However, under the influence of hydrogen, deformation twinning take place after point D in the $PdH_{0.1}$ sample, as shown in Fig. 7.3(d) D, leading to a smoother stress response afterwards. Also, the nucleation of deformation twinning also released large

amount of accumulated stresses, leading to a large drop in stress-strain curve.

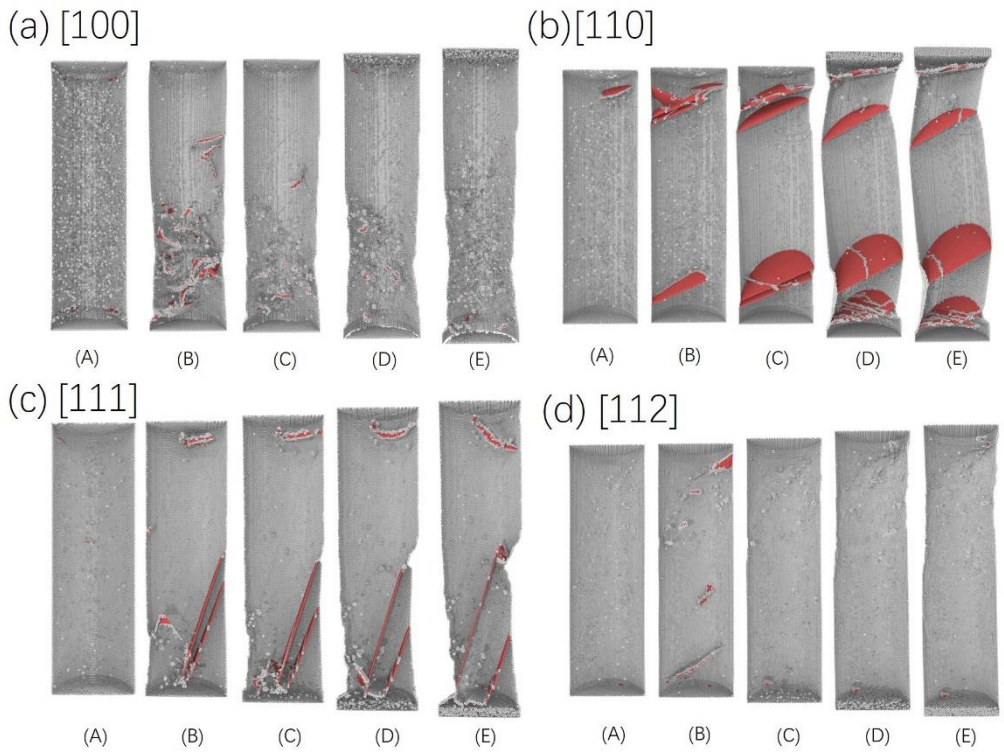

Figure 7.2 Snapshots show for the plasticity response of the pure Pd pillars under tension (T=300K). The pillars are split into half and only half of them are shown.

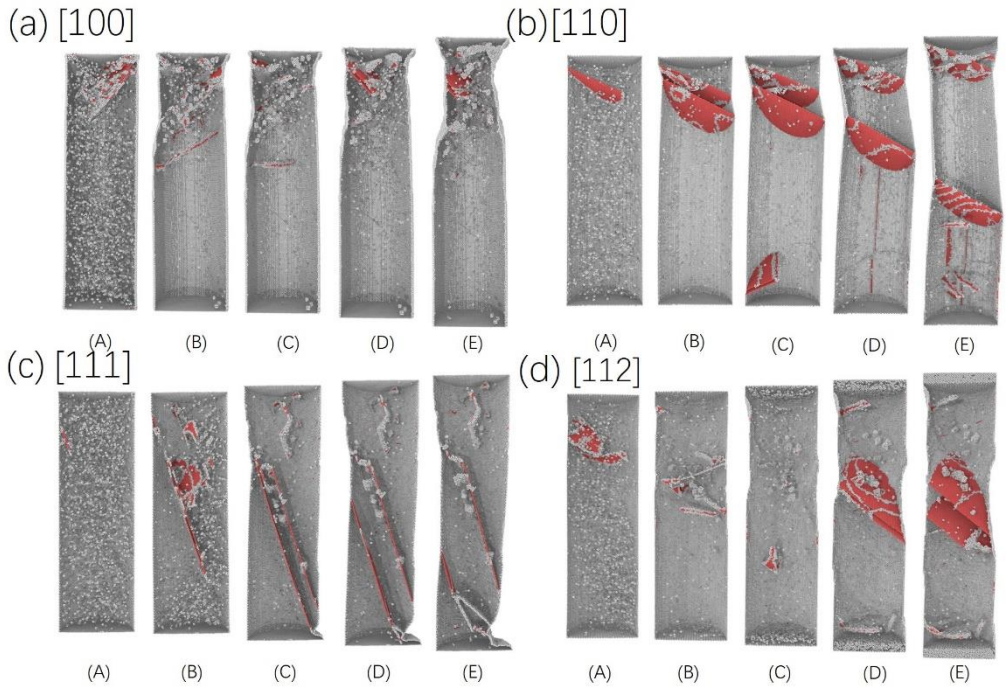

Figure 7.3 Snapshots show for the plasticity response of the PdH0.1 pillars under tension (T=300K). The pillars are split into half and only half of them are shown.

7.5 Generalized Stacking Fault Energy and Schmid Factors

In a broader sense, there are competitions between full dislocations, partial dislocations, and deformation twins. To explain the results, Schmid factor and generalized stacking fault energy are used to explain the influences. The information of Schmid factors (SF) and generalized stacking fault energies (GSFE) and observed deformation mechanisms for the pillars are demonstrated in Table 7.1. The priority between the mechanisms also depends on many factors including the temperature, strain rate, orientation of side surface, deformation load etc. From section 3.2, it is observed that during the tensile deformation in pure Pd samples, twins are nucleated in [110] and [111] pillars, in which the same condition is observed in Ni and Cu[182, 183]. In [100] direction, full

dislocations are nucleated. And in [112] pillar, partial slips are observed. If the SF of the leading partial is larger than the SF of the trailing partial, twin or partial dislocations will appear. It will be difficult for the trailing partial to nucleate. This is the case for [110], [111], and [112] oriented pillars. In the [001] pillar case, the SF of leading partial has a smaller value, leading to a difficulty in nucleation of dislocation. Therefore, the yield stress of it is the highest among all the pillars. In the compression case, values of SF for leading and trailing partial will be reversed, compare to the tension case. The corresponding yield stress in [001] orientation will be the lowest. Schmid factor can offer reliable information about the value of yield stress, the competition between partial slip (including deformation twinning) and full slip. Number of slip systems can offer information about how many sources are available for dislocation nucleation. Larger quantities of slip systems can offer more frequent dislocation nucleation events to release the stresses in the pillar. On the other hand, it increased the chance for dislocation interactions. Hydrogen inclusion has no influence on Schmid factor, which is a geometric concept.

Under the influence of hydrogen, the partial dislocations in [001] pillar are nucleated, and the twinability of [112] pillar is enhanced. The enhancement of the twin formation ability can be explained by the generalized stacking fault energy curve, as shown in Fig. 7.4. In lower right corner of Fig. 7.4, the GSFE of Cu is shown, and γ_U is the unstable stacking fault energy, γ_I is the (intrinsic) stacking fault energy, γ_{UT} is the unstable twin formation energy, and γ_T is the twin formation energy. The twinability has been discussed extensively in literature[176]. It was suggested that low ratios of γ_I/γ_U, high value of $\gamma_{UT} - \gamma_U$ favor twinning[87]. The values of characteristic energies are calculated and listed in Table 7.2. According to the first criteria, i.e. low ratios of γ_I/γ_U, the observation in [112] pillars are well explained. Hydrogen inclusion decreased the ratios of γ_I/γ_U, thus increased the twinability of the pillars. The reason why the $\gamma_{UT} - \gamma_U$ criteria doesn't work well might due to fact that the γ_{UT} is not well characterized by the potential force field, as shown in the Fig. 7.4.

Table 7.1. Summary of Schmid factor and Generalized stacking fault energy analysis of nanopillars.

Orientation	Slip System	Schmid Factor of leading partial	Schmid Factor of trailing partial	Predict by SF	Predict by SF and GSFE	Observed
[001] Pure	8	0.24	0.47	Full Slip	Full Slip	Full Slip
[110] Pure	4	0.47	0.24	Twin/Partial Slip	Twin	Twin
[111] Pure	6	0.31	0.16	Twin/Partial Slip	Twin	Twin
[112] Pure	2	0.31	0.16	Twin/Partial Slip	Twin	Partial
[001] PdH	8	0.24	0.47	Full Slip	Full Slip	Full+Partial
[110] PdH	4	0.47	0.24	Twin/Partial Slip	Twin	Twin
[111] PdH	6	0.31	0.16	Twin/Partial Slip	Twin	Twin
[112] PdH	2	0.31	0.16	Twin/Partial Slip	Twin	Twin

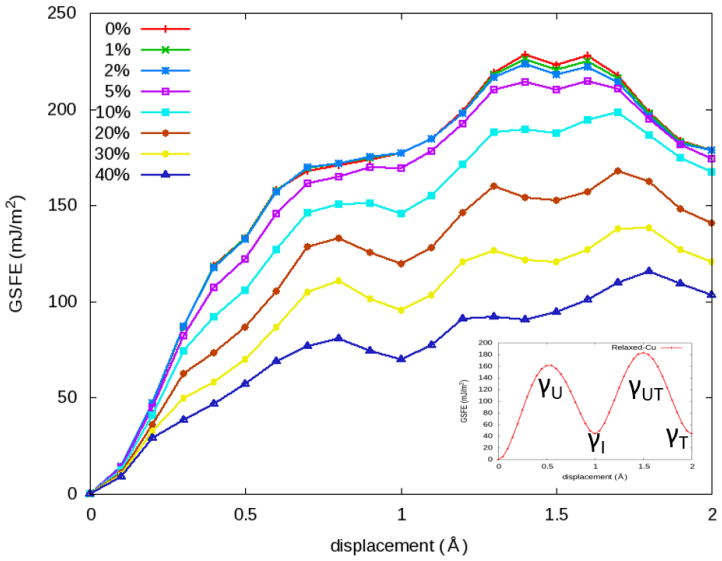

Figure 7.4 Generalized stacking fault energy as a function of hydrogen concentration in Pd.

Table 7.2. Data obtained from Generalized stacking fault energy curve.

H%	USF	SF	UTF	TF	I/U	UT-U
0%	173.776	177.306	228.448	178.728	1.020314	57.565
1%	174.708	177.056	225.931	178.866	1.01344	54.404
2%	175.098	177.149	223.474	178.759	1.011713	51.744
5%	169.659	169.125	214.413	174.071	0.996853	49.215
10%	151.287	145.485	198.279	167.542	0.961649	47.568
20%	133.008	119.402	167.773	140.749	0.897705	34.765
30%	110.565	95.6818	138.401	120.67	0.86539	27.193
40%	80.9409	69.9567	115.739	103.54	0.864294	28.8111

7.6 Strain Rate Concern and Activation Volume

It is well known that Molecular Dynamics will over-estimate the value of yield stresses for metals because of the very high strain rate[78]. To link the value of yield stress calculated in MD with the values in experiments, activation volume, which is the derivative of activation free energy with respect to stress, is critical. Since it measures the sensitivity of nucleation rate to stress, it is useful to resolve the timescale issue between simulation and experiment.

The effect of activation volume on the dislocation nucleation stress is given

$$\sigma = \frac{Q^*}{\hat{\Omega}} - \frac{k_B T}{\hat{\Omega}} \ln \frac{k_B T N \nu_0}{E \dot{\epsilon} \hat{\Omega}} \tag{7.1}$$

Here $\hat{\Omega}$ is the activation volume, k_B is the Boltzmann constant, ν_0 is the attempt frequency for dislocation movement, $\dot{\epsilon}$ is the strain rate, N is number of atoms, E is the youngs modulus, and Q* is the nucleation barrier in the absence of applied stress within the linear approximation of stress-dependent activation energy. The first term $\frac{Q^*}{\hat{\Omega}}$ is the athermal nucleation stress. The pre-factor of the second term $\frac{k_B T}{\hat{\Omega}}$ is representing the stress unit. $k_B T N \nu_0$ is the rate of energy exchange of the candidate nucleation sites with the thermal reservoir, and $E \dot{\epsilon} \hat{\Omega}$ is the rate of activation energy reduction caused by the mechanical load. The ratio between these two terms determines the competition between

thermal and mechanical effects in determining the nucleation stress reduction due to thermal fluctuations. Hydrogen influence on the activation volume in Ni single crystal has been calculated[79]. However, there is no related work on Pd so far.

7.7 Summary

Molecular dynamics simulations are applied to study the tension of Pd nanopillars with different orientations and with the influence of 10% atomic ratio of H. For the four different orientations studied, different plastic deformation mechanisms are observed. In [001]-oriented pillars, full dislocations are the main plastic deformation mechanism. In the [112]-oriented pillars, partial and full dislocation slip are the main mechanism. Both [001] and [112] pillars are dominated by dislocation starvation, so that more serrated flow stresses are found. Twin formation are predominant in the [110], [111]-oriented pillars, leading to frequent dislocation interactions and smaller fluctuations of the flow stress after yielding. With the hydrogen inclusion, the young's modulus, flow stresses, and the fluctuation of flow stresses for samples in all four orientations are decreased. With the influence of hydrogen, partial dislocations are nucleated at 18% strain in [100] oriented sample, but play as a minor role. In [112] oriented sample, hydrogen has helped the nucleation of twin structures at 15% strain, and then twin deformation has taken over than full dislocation slip. According to the general planar fault energy curve, the hydrogen inclusion has decreased the ratio between intrinsic stacking fault energy and unstable stacking fault energy, leading to higher twinability.

8. SUMMARY AND FUTURE RESEARCH

8.1 Summary

We have completed studies on five key topics within this thesis, below we discuss their impact and implications.

In chapter 3, a solid database of thermomechanical properties is built, interesting findings are found in thermal data and mechanical data. Diffusion activation energy has been determined as a function of hydrogen content, crystal pre-melting has also been observed. The results can serve as input or constitutive laws for use in solid mechanics, for discretized dislocation dynamics (DDD) and for finite element method (FEM)[184] based engineering mechanics studies.

In chapter 4 and 5, two critical and long-lasting issues within the context of hydrogen embrittlement and fracture mechanics are quantitatively resolved. First is the tension/compression anisotropic diffusion with accounting the influence of temperature and hydrogen content explicitly. The second one is vacancy crowding phenomenon under strain. Results indicate that the hydrogen crowding only happens at large hydrogen concentrations. As local hydrogen combined with vacancies and formed voids, the conventional HELP mechanics will fail, as dislocations are obstructed by them. Indications are valuable for energy applications, e.g. fuel cells and hydrogen purification, where high temperatures are involved. The results can be easily transferred to the study of other platinum group metals. The technological impact is significant since they are the rarest elements and the most widely used catalysts.

In chapter 6, we created a novel hybrid structure and associated nanoindentation simulation schemes are designed smartly to reveal the in-depth details of local mechanical properties. The combined effects of hydrogen aggregation and coherent twin boundaries have given the local region around boundaries unique properties. Dislocation nucleation are harder in this region, where the young's moduli and hardness of this region is lower. This dislocation entanglement between dislocations grown in different <110> directions

are forming complex networks beneath the indenter. Besides, twin boundaries are serving as defect sinks and hydrogen sinks. In short, the local properties of hydrogenated coherent twin boundaries are firstly carried out by simulation nanoindentation.

In chapter 7, the finale of this thesis is a cutting-edge topic in atomistic mechanics. First, we discussed the slip/twin competition in Pd, which is never discussed in the literature. We observed that the influence of hydrogen has changed the balance of this competition. A review of atomistic deformation mechanisms is done in this work. Generalized stacking fault energy curve for Pd under the influence of H is calculated to explain the twinability enhancement observed in the sample. It has deep impact in nano-electro-mechanical-systems (NEMS). For many catalytical and functional application[185] of nanopillars and nanowires, this study can be beneficial.

8.2 Future Directions

With the new knowledge generated through this thesis and a thorough investigation of the current state of the literature, I suggest the following future research topics to consider

- Phase distribution of alpha and beta phase should be fully understood. In this thesis, the phase distribution/ordering is not discussed. In future study, extra attention need to be paid in here. Since MD might have the wrong configuration to start with at the beginning, if one has limited knowledge on phase distribution.
- With decent mechanics background about the flaws in current constitutive laws compare to the atomistic details, multiscale simulations (concurrent or hierarchical) can be another direction. However, it is very risky since many atomistic microevents might be difficult to describe using analytical expressions and to be add into constitutive functions. One should only start with elastic fracture mechanics based simulations. For non-linear regions, water is still too deep for materials scientist.
- Stress induced phase transition in the metal-hydrogen phase diagram. This is highly possible, especially transitional metal, e.g. Fe and Ni, where magnetism plays important role for stability. Since their phase diagram tend to be very complicated, it

is possible that stress induced phase change might convert the previously ductile phase into a much softer or brittle phase. To prove this hypothesis, one should extend phase diagram calculations into another dimension, i.e. pressure. This could be done by density functional theory combined with Monte Carlo simulations[52].

- For adsorption related issues, one might consider DFT based constant chemical potential Monte Carlo methods.

REFERENCES

1. V. S. Raja and T. Shoji, Stress corrosion cracking : theory and practice. edited by V.S. Raja and Tetsuo Shoji. (Oxford ; Philadelphia : Woodhead Publishing, 2011., 2011).
2. S. B. Gesari, M. E. Pronsato and A. Juan, International Journal of Hydrogen Energy **34** (8), 3511-3518 (2009).
3. R. Kirchheim, Progress in Materials Science **32** (4), 261-325 (1988).
4. H. M. Lawler and D. R. Trinkle, Physical Review B **82** (17), 172101 (2010).
5. R. B. McLellan and L. Yang, Acta Metallurgica et Materialia **43** (6), 2463-2467 (1995).
6. L. L. Jewell and B. H. Davis, Applied Catalysis A: General **310**, 1-15 (2006).
7. M. Johansson, E. Skúlason, G. Nielsen, S. Murphy, R. M. Nielsen and I. Chorkendorff, Surface Science **604** (7–8), 718-729 (2010).
8. T. Mütschele and R. Kirchheim, Scripta Metallurgica **21** (2), 135-140 (1987).
9. R. P. Gangloff and B. P. Somerday, Gaseous hydrogen embrittlement of materials in energy technologies. edited by Richard P. Gangloff and Brian P. Somerday. (Cambridge, UK ; Phildelphia, PA : Woodhead Publishing, 2012., 2012).
10. J. Song and W. A. Curtin, Acta Materialia **59** (4), 1557-1569 (2011).
11. J. Song and W. A. Curtin, Nat Mater **12** (2), 145-151 (2013).
12. J. E. Angelo, N. R. Moody and M. I. Baskes, Modelling and Simulation in Materials Science and Engineering **3** (3), 289 (1995).
13. B. D. Morreale, M. V. Ciocco, R. M. Enick, B. I. Morsi, B. H. Howard, A. V. Cugini and K. S. Rothenberger, Journal of Membrane Science **212** (1–2), 87-97 (2003).
14. J. RaviPrakash, A. H. McDaniel, M. Horn, L. Pilione, P. Sunal, R. Messier, R. T. McGrath and F. K. Schweighardt, Sensors and Actuators B: Chemical **120** (2), 439-446 (2007).
15. Y. Li and Y.-T. Cheng, International Journal of Hydrogen Energy **21** (4), 281-291 (1996).
16. W. E. Vargas, I. Rojas, D. E. Azofeifa and N. Clark, Thin Solid Films **496** (2), 189-196 (2006).

17. W. Lin, R. G. Nuzzo and G. S. Girolami, Journal of the American Chemical Society **118** (25), 5988-5996 (1996).
18. P. Quaino and E. Santos, Langmuir **31** (2), 858-867 (2015).
19. R. J. Highmore, W. C. Shih, R. E. Somekh and J. E. Evetts, Journal of Vacuum Science & Technology A **9** (4), 2123-2127 (1991).
20. S.-W. Kim, J. Park, Y. Jang, Y. Chung, S. Hwang, T. Hyeon and Y. W. Kim, Nano Letters **3** (9), 1289-1291 (2003).
21. J. Cookson, Platinum Metals Review **56** (2), 83-98 (2012).
22. A. Pundt and R. Kirchheim, Annu Rev Mater Res **36**, 555-608 (2006).
23. T. B. Flanagan and W. A. Oates, Annu Rev Mater Sci **21**, 269-304 (1991).
24. F. Manchester, A. San-Martin and J. Pitre, Journal of phase equilibria **15** (1), 62-83 (1994).
25. S. H. Goods and S. E. Guthrie, Scripta Metallurgica Et Materialia **26** (4), 561-565 (1992).
26. T. Mitsui, M. K. Rose, E. Fomin, D. F. Ogletree and M. Salmeron, Nature **422** (6933), 705-707 (2003).
27. A. L. Cabrera and R. Aguayo-Soto, Catalysis Letters **45** (1), 79-83 (1997).
28. S. Asano and R. Otsuka, Scripta Metallurgica **10** (11), 1015-1020 (1976).
29. D. P. Abraham and C. J. Altstetter, Metallurgical and Materials Transactions A **26** (11), 2849-2858 (1995).
30. A. Kimura and H. K. Birnbaum, Scripta Metallurgica **21** (1), 53-57 (1987).
31. H. K. Birnbaum and P. Sofronis, Materials Science and Engineering: A **176** (1), 191-202 (1994).
32. R. A. Oriani, Berichte der Bunsengesellschaft für physikalische Chemie **76** (8), 848-857 (1972).
33. M. Seita, J. P. Hanson, S. Gradečak and M. J. Demkowicz, Nat Commun **6** (2015).
34. A. Barnoush and H. Vehoff, Acta Materialia **58** (16), 5274-5285 (2010).
35. I. M. Robertson, Engineering Fracture Mechanics **68** (6), 671-692 (2001).
36. P. J. Ferreira, I. M. Robertson and H. K. Birnbaum, Acta Materialia **47** (10),

2991-2998 (1999).

37. T. J. Marrow, C. A. Hippsley and J. E. King, Acta Metallurgica et Materialia **39** (6), 1367-1376 (1991).

38. Y. Murakami, T. Kanezaki and Y. Mine, Metallurgical and Materials Transactions A **41** (10), 2548-2562 (2010).

39. M. R. Louthan, Journal of Failure Analysis and Prevention **8** (3), 289-307 (2008).

40. A. Shabaev, D. A. Papaconstantopoulos, M. J. Mehl and N. Bernstein, Physical Review B **81** (18), 184103 (2010).

41. L. E. Isaeva, D. I. Bazhanov, E. I. Isaev, S. V. Eremeev, S. E. Kulkova and I. A. Abrikosov, International Journal of Hydrogen Energy **36** (1), 1254-1258 (2011).

42. H. Grönbeck and V. P. Zhdanov, Physical Review B **84** (5), 052301 (2011).

43. X. Zhou, D. Marchand, D. L. McDowell, T. Zhu and J. Song, Physical Review Letters **116** (7), 075502 (2016).

44. S. P. Lynch, Metallurgical and Materials Transactions A **44** (3), 1209-1229 (2013).

45. S. P. Lynch, Acta Metallurgica **36** (10), 2639-2661 (1988).

46. W. W. Gerberich, R. A. Oriani, M. J. Lji, X. Chen and T. Foecke, Philosophical Magazine A **63** (2), 363-376 (1991).

47. T. Zhu, J. Li, S. Ogata and S. Yip, MRS Bulletin **34** (3), 167-172 (2009).

48. T. Zhu and J. Li, Progress in Materials Science **55** (7), 710-757 (2010).

49. Y. Tang and J. A. El-Awady, Physical Review B **86** (17), 174102 (2012).

50. D. Xie, S. Li, M. Li, Z. Wang, P. Gumbsch, J. Sun, E. Ma, J. Li and Z. Shan, Nature Communications **7**, 13341 (2016).

51. S. Li, Y. Li, Y.-C. Lo, T. Neeraj, R. Srinivasan, X. Ding, J. Sun, L. Qi, P. Gumbsch and J. Li, International Journal of Plasticity **74**, 175-191 (2015).

52. M. Asta, D. de Fontaine, M. van Schilfgaarde, M. Sluiter and M. Methfessel, Physical Review B **46** (9), 5055-5072 (1992).

53. Y. Li and G. Wahnström, Physical Review B **46** (22), 14528-14542 (1992).

54. W. Zhong, Y. Cai and D. Toma´nek, Physical Review B **46** (13), 8099-8108 (1992).

55. W. H. Johnson, Proceedings of the Royal Society of London **23** (156-163), 168-179 (1874).
56. J. Völkl and G. Alefeld, in Hydrogen in Metals I: Basic Properties, edited by G. Alefeld and J. Völkl (Springer Berlin Heidelberg, Berlin, Heidelberg, 1978), pp. 321-348.
57. M. J. Gillan, Journal of Physics C: Solid State Physics **19** (31), 6169 (1986).
58. H. H. P. a. T. Cagin.
59. D. E. Spearot, M. A. Tschopp, K. I. Jacob and D. L. McDowell, Acta Materialia **55** (2), 705-714 (2007).
60. M. A. Tschopp and D. L. McDowell, Philosophical Magazine **87** (25), 3871-3892 (2007).
61. M. A. Tschopp and D. L. McDowell, Philosophical Magazine **87** (22), 3147-3173 (2007).
62. M. A. Tschopp, G. J. Tucker and D. L. McDowell, Acta Materialia **55** (11), 3959-3969 (2007).
63. M. A. Tschopp and D. L. McDowell, Applied Physics Letters **90** (12), 121916 (2007).
64. M. A. Tschopp and D. L. McDowell, Journal of Materials Science **42** (18), 7806-7811 (2007).
65. M. A. Tschopp, D. E. Spearot and D. L. McDowell, Modelling and Simulation in Materials Science and Engineering **15** (7), 693-709 (2007).
66. M. A. Tschopp and D. L. McDowell, Journal of the Mechanics and Physics of Solids **56** (5), 1806-1830 (2008).
67. M. A. Tschopp and D. L. McDowell, International Journal of Plasticity **24** (2), 191-217 (2008).
68. M. A. Tschopp and D. L. McDowell, Scripta Materialia **58** (4), 299-302 (2008).
69. M. A. Tschopp, D. E. Spearot and D. L. McDowell, in Dislocations in Solids, edited by J. P. Hirth (Elsevier, 2008), Vol. Volume 14, pp. 43-139.
70. M. A. Tschopp, G. J. Tucker and D. L. McDowell, Computational Materials Science **44** (2), 351-362 (2008).

71. M. A. Tschopp, B. B. Bartha, W. J. Porter, P. T. Murray and S. B. Fairchild, Metallurgical and Materials Transactions A **40** (10), 2363-2368 (2009).
72. M. A. Tschopp, M. F. Horstemeyer, F. Gao, X. Sun and M. Khaleel, Scripta Materialia **64** (9), 908-911 (2011).
73. M. A. Tschopp, K. N. Solanki, F. Gao, X. Sun, M. A. Khaleel and M. F. Horstemeyer, Physical Review B **85** (6), 064108 (2012).
74. M. A. Tschopp, K. N. Solanki, M. I. Baskes, F. Gao, X. Sun and M. F. Horstemeyer, Journal of Nuclear Materials **425** (1–3), 22-32 (2012).
75. T. Zhu, W. Yang and T. Guo, Acta Materialia **44** (8), 3049-3058 (1996).
76. Z. Zeng, X. Li, L. Lu and T. Zhu, Acta Materialia **98**, 313-317 (2015).
77. X. H. Liu, L. Zhong, S. Huang, S. X. Mao, T. Zhu and J. Y. Huang, ACS Nano **6** (2), 1522-1531 (2012).
78. T. Zhu, J. Li, A. Samanta, A. Leach and K. Gall, Phys Rev Lett **100** (2), 025502 (2008).
79. M. Wen and Z. Li, Computational Materials Science **54**, 28-31 (2012).
80. M. Wen, L. Zhang, B. An, S. Fukuyama and K. Yokogawa, Physical Review B **80** (9) (2009).
81. J. P. Chateau, D. Delafosse and T. Magnin, Acta Materialia **50** (6), 1507-1522 (2002).
82. J. P. Chateau, D. Delafosse and T. Magnin, Acta Materialia **50** (6), 1523-1538 (2002).
83. C. Hwang and I. M. Bernstein, Scripta Metallurgica **17** (11), 1299-1304 (1983).
84. C. Hwang and I. M. Bernstein, Acta Metallurgica **34** (6), 1001-1010 (1986).
85. S. Taketomi, R. Matsumoto and N. Miyazaki, Journal of Materials Research **26** (10), 1269-1278 (2011).
86. J. Tien, A. W. Thompson, I. M. Bernstein and R. J. Richards, Metallurgical Transactions A **7** (6), 821-829 (1976).
87. I. J. Beyerlein, X. H. Zhang and A. Misra, in Annual Review of Materials Research, Vol 44, edited by D. R. Clarke (Annual Reviews, Palo Alto, 2014), Vol. 44, pp. 329-363.

88. N. Li, J. Wang, A. Misra, X. Zhang, J. Y. Huang and J. P. Hirth, Acta Materialia **59** (15), 5989-5996 (2011).
89. N. Li, J. Wang, J. Y. Huang, A. Misra and X. Zhang, Scripta Materialia **64** (2), 149-152 (2011).
90. J. Li, K. J. Van Vliet, T. Zhu, S. Yip and S. Suresh, Nature **418** (6895), 307-310 (2002).
91. K. J. Van Vliet, J. Li, T. Zhu, S. Yip and S. Suresh, Physical Review B **67** (10) (2003).
92. T. Zhu, J. Li and S. Yip, Physical Review Letters **93** (2), 025503 (2004).
93. T. Zhu, J. Li, K. J. Van Vliet, S. Ogata, S. Yip and S. Suresh, Journal of the Mechanics and Physics of Solids **52** (3), 691-724 (2004).
94. J. Li, MRS Bulletin **32** (2), 151-159 (2007).
95. L. Lu, M. Dao, T. Zhu and J. Li, Scripta Materialia **60** (12), 1062-1066 (2009).
96. X. Zhou and J. Song, Materials Letters **196**, 123-127 (2017).
97. H. Van Swygenhoven, P. M. Derlet and A. G. Froseth, Nat Mater **3** (6), 399-403 (2004).
98. H. Van Swygenhoven and P. M. Derlet, in Dislocations in Solids, edited by J. P. Hirth (Elsevier, 2008), Vol. Volume 14, pp. 1-42.
99. M. S. Daw and M. I. Baskes, Physical Review Letters **50** (17), 1285-1288 (1983).
100. Y. Mishin, M. J. Mehl, D. A. Papaconstantopoulos, A. F. Voter and J. D. Kress, Physical Review B **63** (22), 224106 (2001).
101. X. W. Zhou, J. A. Zimmerman, B. M. Wong and J. J. Hoyt, Journal of Materials Research **23** (03), 704-718 (2008).
102. S. Plimpton, Journal of Computational Physics **117** (1), 1-19 (1995).
103. W. H. Press, Numerical recipes : the art of scientific computing. 3rd ed. William H. Press [and others]. (Cambridge, UK ; New York : Cambridge University Press, 2007. 3rd ed., 2007).
104. T. P. Jones and K. G. Hall, Metrologia **15** (3), 161 (1979).
105. P. Vinet, J. R. Smith, J. Ferrante and J. H. Rose, Physical Review B **35** (4), 1945-

1953 (1987).
106. M. Deutges, H. P. Barth, Y. Chen, C. Borchers and R. Kirchheim, Acta Materialia **82**, 266-274 (2015).
107. P. H. Dederichs and K. Schroeder, Physical Review B **17** (6), 2524-2536 (1978).
108. V. M. Sidorenko, B. F. Kachmar and N. S. Borisova, Soviet materials science : a transl. of Fiziko-khimicheskaya mekhanika materialov / Academy of Sciences of the Ukrainian SSR **9** (5), 500-504 (1975).
109. X. Z. Jonathan A. Zimmerman, Joshua Griffin, Bryan M. Wong and Jeffrey J. Hoyt, SANDIA REPORT (2007).
110. W. G. Hoover, Physical Review A **31** (3), 1695-1697 (1985).
111. F. Yuh and Ō. Nobuyuki, Japanese Journal of Applied Physics **32** (9A), L1256 (1993).
112. Y. Fukai, Journal of Alloys and Compounds **231** (1), 35-40 (1995).
113. H. Osono, T. Kino, Y. Kurokawa and Y. Fukai, Journal of Alloys and Compounds **231** (1), 41-45 (1995).
114. Y. Fukai, Y. Ishii, Y. Goto and K. Watanabe, Journal of Alloys and Compounds **313** (1–2), 121-132 (2000).
115. Y. Fukai, Y. Shizuku and Y. Kurokawa, Journal of Alloys and Compounds **329** (1–2), 195-201 (2001).
116. Y. Fukai, Journal of Alloys and Compounds **356–357**, 263-269 (2003).
117. Y. Fukai, M. Mizutani, S. Yokota, M. Kanazawa, Y. Miura and T. Watanabe, Journal of Alloys and Compounds **356–357**, 270-273 (2003).
118. Y. Fukai, K. Mori and H. Shinomiya, Journal of Alloys and Compounds **348** (1–2), 105-109 (2003).
119. B. D. Adams and A. Chen, Materials Today **14** (6), 282-289 (2011).
120. T. R. Mattsson and A. E. Mattsson, Physical Review B **66** (21), 214110 (2002).
121. M. Militzer, W. P. Sun and J. J. Jonas, Acta Metallurgica et Materialia **42** (1), 133-141 (1994).
122. W. C. Oliver and G. M. Pharr, Journal of materials research **7** (06), 1564-1583 (1992).

123. R. Kirchheim, Scripta Materialia **62** (2), 67-70 (2010).
124. J. M. Wheeler and T. W. Clyne, International Journal of Hydrogen Energy **37** (19), 14315-14322 (2012).
125. B. Amin-Ahmadi, H. Idrissi, R. Delmelle, T. Pardoen, J. Proost and D. Schryvers, Applied Physics Letters **102** (7), 071911 (2013).
126. B. Amin-Ahmadi, D. Connétable, M. Fivel, D. Tanguy, R. Delmelle, S. Turner, L. Malet, S. Godet, T. Pardoen, J. Proost, D. Schryvers and H. Idrissi, Acta Materialia **111**, 253-261 (2016).
127. T. Zhang, Y. Nakagawa, T. Wakasugi, S. Isobe, Y. Wang, N. Hashimoto and S. Ohnuki, ACS Applied Materials & Interfaces **8** (23), 14548-14551 (2016).
128. A. R. Troiano.
129. P. J. Ferreira, I. M. Robertson and H. K. Birnbaum, Acta Materialia **46** (5), 1749-1757 (1998).
130. P. Sofronis and I. M. Robertson, Philosophical Magazine A **82** (17-18), 3405-3413 (2002).
131. D. M. Barnett, G. Wong and W. D. Nix, Acta Metallurgica **30** (11), 2035-2041 (1982).
132. R. J. Asaro and S. Suresh, Acta Materialia **53** (12), 3369-3382 (2005).
133. B. Zhu, R. J. Asaro, P. Krysl, K. Zhang and J. R. Weertman, Acta Materialia **54** (12), 3307-3320 (2006).
134. E. N. Hahn and M. A. Meyers, Materials Science and Engineering: A **646**, 101-134 (2015).
135. L. Lu, T. Zhu, Y. Shen, M. Dao, K. Lu and S. Suresh, Acta Materialia **57** (17), 5165-5173 (2009).
136. K. Lu, Nature Reviews Materials **1**, 16019 (2016).
137. T. Fu, X. Peng, X. Chen, S. Weng, N. Hu, Q. Li and Z. Wang, Scientific Reports **6**, 35665 (2016).
138. R. Seymour, A. Hemeryck, K.-i. Nomura, W. Wang, R. K. Kalia, A. Nakano and P. Vashishta, Applied Physics Letters **104** (14), 141904 (2014).
139. T. Tsuru, Y. Kaji, D. Matsunaka and Y. Shibutani, Physical Review B **82** (2)

(2010).
140. S. Qu and H. Zhou, Nanotechnology **21** (33), 335704 (2010).
141. A. K. Nair, D. Farkas and R. D. Kriz, (2008).
142. K. J. Kim, J. H. Yoon, M. H. Cho and H. Jang, Materials Letters **60** (28), 3367-3372 (2006).
143. M. A. Tschopp, S. P. Coleman and D. L. McDowell, Integrating Materials and Manufacturing Innovation **4** (1), 1-14 (2015).
144. I. Muhammad, H. Fayyaz, R. Muhammad and S. A. Ahmad, Chinese Physics B **21** (11), 116201 (2012).
145. T. Schneider and E. Stoll, Physical Review B **17** (3), 1302-1322 (1978).
146. S. Alexander, Modelling and Simulation in Materials Science and Engineering **18** (1), 015012 (2010).
147. J. R. Greer and J. T. M. De Hosson, Progress in Materials Science **56** (6), 654-724 (2011).
148. V. P. Menon and C. R. Martin, Analytical Chemistry **67** (13), 1920-1928 (1995).
149. Y. Wu, J. Xiang, C. Yang, W. Lu and C. M. Lieber, Nature **430** (6995), 61-65 (2004).
150. T. M. Whitney, P. C. Searson, J. S. Jiang and C. L. Chien, Science **261** (5126), 1316-1319 (1993).
151. W. F. Paxton, K. C. Kistler, C. C. Olmeda, A. Sen, S. K. St. Angelo, Y. Cao, T. E. Mallouk, P. E. Lammert and V. H. Crespi, Journal of the American Chemical Society **126** (41), 13424-13431 (2004).
152. G. A. Ozin, I. Manners, S. Fournier-Bidoz and A. Arsenault, Advanced Materials **17** (24), 3011-3018 (2005).
153. M. D. Uchic, D. M. Dimiduk, J. N. Florando and W. D. Nix, Science **305** (5686), 986 (2004).
154. D. M. Dimiduk, M. D. Uchic, S. I. Rao, C. Woodward and T. A. Parthasarathy, Modelling and Simulation in Materials Science and Engineering **15** (2), 135 (2007).
155. K. S. Ng and A. H. W. Ngan, Acta Materialia **56** (8), 1712-1720 (2008).
156. Z.-J. Wang, Q.-J. Li, Z.-W. Shan, J. Li, J. Sun and E. Ma, Applied Physics Letters

100 (7), 071906 (2012).

157. W. Z. Han, L. Huang, S. Ogata, H. Kimizuka, Z. C. Yang, C. Weinberger, Q. J. Li, B. Y. Liu, X. X. Zhang, J. Li, E. Ma and Z. W. Shan, Advanced Materials **27** (22), 3385-3390 (2015).

158. J. R. Greer, W. C. Oliver and W. D. Nix, Acta Materialia **53** (6), 1821-1830 (2005).

159. H. Bei, S. Shim, E. P. George, M. K. Miller, E. G. Herbert and G. M. Pharr, Scripta Materialia **57** (5), 397-400 (2007).

160. M. B. Lowry, D. Kiener, M. M. LeBlanc, C. Chisholm, J. N. Florando, J. W. Morris Jr and A. M. Minor, Acta Materialia **58** (15), 5160-5167 (2010).

161. S. Lee, J. Jeong, Y. Kim, S. M. Han, D. Kiener and S. H. Oh, Acta Materialia **110**, 283-294 (2016).

162. J. J. Gilman, Micromechanics of flow in solids. (McGraw-Hill, 1969).

163. C. Chisholm, H. Bei, M. B. Lowry, J. Oh, S. A. Syed Asif, O. L. Warren, Z. W. Shan, E. P. George and A. M. Minor, Acta Materialia **60** (5), 2258-2264 (2012).

164. T. Zhu, J. Li, A. Samanta, H. G. Kim and S. Suresh, Proceedings of the National Academy of Sciences **104** (9), 3031-3036 (2007).

165. I. Galanakis, N. Papanikolaou and P. H. Dederichs, Surface Science **511** (1), 1-12 (2002).

166. V. Vítek, Philosophical Magazine **18** (154), 773-786 (1968).

167. J. R. Rice, Journal of the Mechanics and Physics of Solids **40** (2), 239-271 (1992).

168. J. P. Hirth and J. Lothe, Theory of Dislocations. (Krieger Publishing Company, 1982).

169. W. D. Callister and D. G. Rethwisch, Materials science and engineering. (John Wiley & Sons NY, 2011).

170. A. H. Cottrell, American Journal of Physics **22** (4), 242-243 (1954).

171. M. D. Uchic, P. A. Shade and D. M. Dimiduk, Annu Rev Mater Res **39** (1), 361-386 (2009).

172. A. S. Schneider, D. Kaufmann, B. G. Clark, C. P. Frick, P. A. Gruber, R. Mönig,

O. Kraft and E. Arzt, Physical Review Letters **103** (10), 105501 (2009).

173. S. Brochard, P. Beauchamp and J. Grilhé, Philosophical Magazine A **80** (3), 503-524 (2000).

174. A. Barnoush and H. Vehoff, International Journal of Materials Research **97** (9), 1224-1229 (2006).

175. K. N. Solanki, M. A. Tschopp, M. A. Bhatia and N. R. Rhodes, Metallurgical and Materials Transactions A **44** (3), 1365-1375 (2013).

176. C. R. Weinberger and W. Cai, Journal of Materials Chemistry **22** (8), 3277-3292 (2012).

177. Z. You, X. Li, L. Gui, Q. Lu, T. Zhu, H. Gao and L. Lu, Acta Materialia **61** (1), 217-227 (2013).

178. J. D. Honeycutt and H. C. Andersen, The Journal of Physical Chemistry **91** (19), 4950-4963 (1987).

179. K. Lee, M. Yuan and J. Wilcox, The Journal of Physical Chemistry C **119** (34), 19642-19653 (2015).

180. H. M. Lee, Metallurgical Transactions A **7** (3), 431-433 (1976).

181. V. Antonov, I. Belash, V. Y. Malyshev and E. Ponyatovsky, Platinum Metals Review **28** (4), 158-163 (1984).

182. W. Liang and M. Zhou, Physical Review B **73** (11), 115409 (2006).

183. H. S. Park, K. Gall and J. A. Zimmerman, Physical Review Letters **95** (25), 255504 (2005).

184. D. L. McDowell, International Journal of Plasticity **26** (9), 1280-1309 (2010).

185. A. Chen and C. Ostrom, Chemical Reviews **115** (21), 11999-12044 (2015).